Algorithm theoretical basis for Version 3 TEMPO Level 0-1 processor

Heesung Chong[1], Xiong Liu[1], John Houck[1], David E. Flittner[2], James Carr[3], Weizhen Hou[1], John E. Davis[1], Raid M. Suleiman[1], Kelly Chance[1], Nischal Mishra[4], Christopher Chan Miller[1,5], Gonzalo González Abad[1], Brian Baker[6], James Lasnik[6], Dennis Nicks[6], Juseon Bak[1,7], Caroline R. Nowlan[1], Huiqun Wang[1], Junsung Park[1], Jean Fitzmaurice[1], and Laurel Carpenter[1]

[1]Atomic and Molecular Physics Division, Center for Astrophysics | Harvard & Smithsonian, Cambridge, MA, USA

[2]NASA Langley Research Center, Hampton, VA, USA.

[3]Carr Astronautics, Greenbelt, MD, USA.

[4]Applied Physics Laboratory, Johns Hopkins University, Laurel, MD, USA.

[5]Harvard School of Engineering and Applied Sciences, Harvard University, Cambridge, MA, USA

[6]Space and Mission Systems, BAE Systems, Inc., Boulder, CO, USA

[7]Pusan National University, Busan, South Korea

Corresponding author: Heesung Chong (hee_sung.chong@cfa.harvard.edu)

Key Points:

- This article describes the Level 0-1 processor for the Tropospheric Emissions: Monitoring of Pollution (TEMPO) instrument.
- Calibration key data from pre-launch instrument characterization are presented.
- In-flight calibration results are discussed.

Abstract

The Tropospheric Emissions: Monitoring of Pollution (TEMPO) instrument is the first space-borne hyperspectral spectrometer that measures backscattered sunlight over North America in a geostationary orbit. The two charge-coupled device (CCD) detectors of TEMPO, with spectral coverages of 293–494 and 538–741 nm and resolutions of 0.53–0.63 nm, are capable of identifying absorption features of key trace gases, including ozone, nitrogen dioxide, formaldehyde, and others. Using a step-and-stare scanning mechanism, the TEMPO instrument measures backscattered Earth radiance spectra hourly during the middle of the day (nominal scans) and every 40 minutes in the early morning and late afternoon (optimized scans) to effectively cover the sunlit portions of the continent, with scans during twilight when permitted by instrument safety constraints. Solar irradiance measurements are also conducted nominally with a weekly frequency. This article describes the Version 3 algorithm for TEMPO Level 1b data processing, which provides radiometrically and spectrally calibrated solar irradiance and Earth radiance spectra as the primary outputs. The processing includes the conversion of digitized Level-0 signals to radiance or irradiance, image navigation and registration for Earth spectra, and spectral calibration. This article also discusses calibration key data derived from pre-launch instrument characterization and in-flight calibration results.

Plain Language Summary

The TEMPO Level 1b products provide solar irradiance and geolocated Earth radiance spectra, essential data for retrieving hourly amounts of key trace gases over North America. The Level 1 spectra are processed from digitized signals stored in the Level 0 products, which are reconstructed using raw data downlinked from the satellite. This article describes the TEMPO Level 0-1 processor from theoretical and practical perspectives.

Keywords: **TEMPO, Level 0-1 processor, calibration**

1 Introduction

The Tropospheric Emissions: Monitoring of Pollution (TEMPO) is NASA's first Earth Venture Instrument (EVI-1) project, led by the Smithsonian Astrophysical Observatory (SAO) since its selection in 2012 (Zoogman et al., 2017). Instrument project management was provided by NASA Langley Research Center (LaRC), and instrument development was conducted by Ball Aerospace and Technologies Corporation (BATC), now part of BAE Systems Inc. After the instrument delivery in November 2018, the TEMPO mission partnered with the satellite provider Maxar in 2019 and the host Intelsat in 2020. The TEMPO instrument was launched on April 7, 2023, onboard the commercial geostationary communications satellite Intelsat-40e (IS-40e) via SpaceX Falcon 9 into a geostationary orbit at 91°W longitude.

The primary purpose of the TEMPO mission is to monitor key atmospheric constituents over North America hourly at high spatial resolution, including ozone (O_3), nitrogen dioxide (NO_2), and formaldehyde (HCHO). The relevant outputs are Level 2 and Level 3 products, which respectively provide column amounts of trace gases at the as-measured and gridded locations. The Level 2 data are derived using solar irradiance and backscattered Earth radiance spectra measured from the TEMPO instrument, stored in the Level 1b products (González Abad et al., 2025; Nowlan et al., 2025; Park et al., 2025; Wang et al., 2025). Therefore, ensuring the quality of the Level 1b data is essential to attaining high-performance Level 2 retrievals.

Once raw data of TEMPO measurements are downlinked and forwarded to the ground system, they are reconstructed to Level 0 data at the Instrument Operations Center (IOC) and formatted at the Science Data Processing Center (SDPC). The digital counts stored in the Level 0 products are then converted to Level 1 data in physical units by the Level 0-1 processor at the SDPC. The TEMPO Level 0-1 processor has been updated since its initial development to incorporate pre-launch calibration key data and instrument characteristics identified from in-flight measurements. The first TEMPO Level 1 products released to the public jointly with other levels of data were in Version 3, which includes Sun and Earth measurements beginning August 1 and 2, 2023, respectively, and dark current data beginning July 21, 2023. In this work, we assign the Level 0-1 processor the same version number as the Level 1b products. This article aims to document the theoretical and practical aspects of the Version 3 TEMPO Level 0-1 processor.

In Section 2, we provide an overview of the TEMPO instrument, the signal flow within the system, and TEMPO operations. Section 3 describes each step of the Level 0-1 processor in detail. Section 4 discusses the verification and optimization of the Level 0-1 processor using in-flight measurements. Section 5 provides a summary.

2 Context

2.1 TEMPO Instrument

Figure 1 shows a schematic diagram of the TEMPO instrument. The optical system comprises a calibration mechanism assembly (CMA), a scan mechanism assembly (SMA), a three-mirror telescope, a grating spectrometer, and a focal plane array (FPA). Focal plane electronics (FPE) and thermal control surfaces (including a sensor heat sink) are integrated alongside TEMPO on the nadir-facing deck of the IS-40e spacecraft, with instrument control electronics (ICE) housed inside the spacecraft.

Blue lines in Figure 1 represent the light paths within the instrument for Sun and Earth exposures. Once light reaches the aperture, it enters through the CMA. The light is then reflected off a scan mirror in the SMA and projected by the three-mirror telescope onto the entrance slit of the Offner-form spectrometer, where it is spectrally dispersed onto the FPA.

The CMA has four selectable positions: (i) open, (ii) closed, (iii) full aperture working diffuser, and (iv) full aperture reference diffuser. The open position is used for Earth exposure. The closed position is configured for dark exposure and other important aspects, including protection and contamination control of the instrument. The working and reference diffusers are used for Sun exposure, with the former employed on a regular basis (weekly, for the current configuration) and the latter utilized every three months to trend any degradation of the working diffuser from radiation exposure and contamination.

The scan mirror employs a two-axis mechanism involving an East-West scan axis and a North-South tilt axis. At the beginning of each Earth scan collection, a slit image is projected on the Earth's surface, aligning the TEMPO field of view (FOV) in the North-South direction. Then, the SMA steps the flat scan mirror from East to West to scan the FOV across the Earth. For nominal operations, the scan mirror is initially positioned at the center of the North-South axis. With gyro compensation enabled, the TEMPO instrument receives gyro bias information from

the spacecraft to compensate for drift in the actual scan mirror motions. The East-West scan is not activated for Sun exposure.

The telescope and the spectrometer are collectively referred to as an opto-mechanical subsystem, which is under active temperature control for high spectral stability. The Schmidt mirror (T2) of the telescope is coated to block out-of-band light, minimizing the amount of stray light within the spectrometer. The other telescope mirrors have ultraviolet (UV)-enhanced aluminum coatings. The spectrometer utilizes a diffraction grating with a groove density of 500 lines mm^{-1}. To mitigate polarization, a quartz wave plate is deployed within the spectrometer.

The FPA has two identically designed charge-coupled device (CCD) detectors: one covers a spectral range of ~293–494 nm (UV to blue), and the other covers a spectral range of ~538–741 nm (green to red to near infrared). For simplicity, we refer to the two CCDs as UV and visible (VIS), respectively. The size of the spectral gap between 494 and 538 nm was determined in design by various factors, including the number of spectral pixels on the CCDs and physical restrictions regarding their spacing. Additionally, there was the need of the scientific community to adequately cover O_3 absorption in VIS wavelengths for lower tropospheric retrievals, while extending the spectral range to 740 nm for vegetation products derived using chlorophyll fluorescence.

The FPA and FPE are collectively referred to as a focal plane subsystem (FPS). The FPS has a read-while-integrating architecture, with the flexibility to specify a desired integration time per frame and the number of co-added frames. The CCDs are passively cooled with a dedicated thermal connection to a cold-biased spacecraft thermal interface and stabilized with a heater on the thermal connection. The FPA is nominally operated at –21°C to reduce and control dark current. The nominal FPE temperature was 42°C during pre-launch testing, and its typical range is 49–52°C on orbit, all of which are well within the operational limits.

Further details regarding the TEMPO instrument can be found in the article by Zoogman et al. (2017), which also provides comprehensive descriptions of the TEMPO implementation, operations, and other aspects. Considering slight updates in certain instrument characteristics made since the work of Zoogman et al. (2017), Table 1 in this article presents a summary of the key characteristics of the TEMPO instrument and measurements, reflecting the as-built instrument.

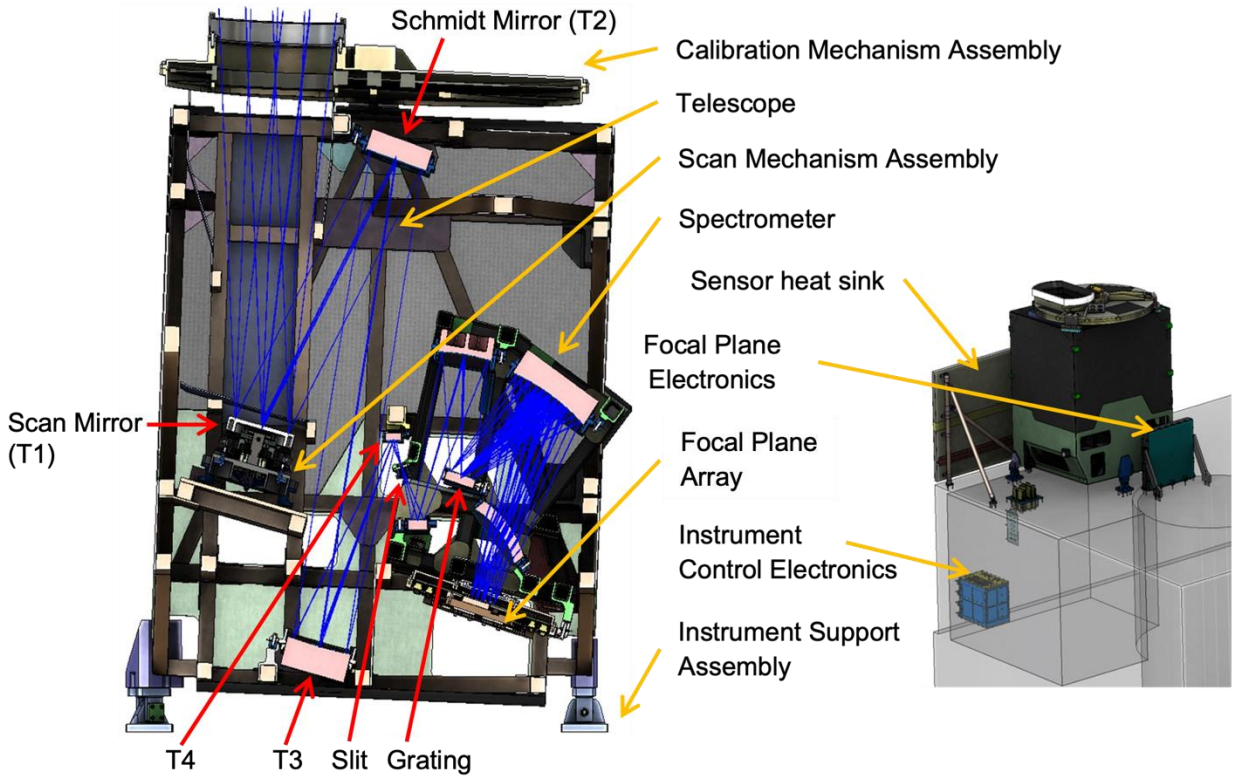

Figure 1. Schematic diagram of the TEMPO instrument.
(Credit: Ball Aerospace and Technologies Corporation, now BAE Systems Inc.)

149 **Table 1.** TEMPO instrument and measurement characteristics.

Volume, Mass	1.4 m × 1.1 m × 1.2 m, 137 kg
Average operating power	138 W
Detector size	Two 2048 (spatial) × 1028 (spectral) detectors
Wavelength range	UV band: ~293–494 nm, VIS band: ~538–741 nm
Spectral resolution	~0.6 nm (full width at half maximum, FWHM) (0.53–0.63 nm)
Spectral sampling	~0.2 nm or ~3 pixels per FWHM (2.7–3.2)
Spectral co-registration[1]	< 0.1 pixel (for UV, VIS, UV/VIS)
Orbit	Geostationary (35,786 km), 91.0°W above Equator
Instantaneous field of view[2]	41.49 μrad (N/S) x 129.20 μrad (E/W)
Modulation transfer function at Nyquist[2]	0.31–0.41 N/S × 0.38–0.49 E/W
Field of regard (FOR)[2,3]	4.87° N/S × 8.66° E/W
Spatial resolution[2]	2.0 km (N/S) × 4.75 km (E/W) at center of FOR
Temporal resolution[4]	~1 hour, ~3-second snapshot per mirror step
Spectra per hour[2,3,4,5]	2036 N/S × 1181 E/W
Spectral maximum signal-to-noise ratio[6]	1372–1394 at 330–340 nm

150 [1]Smile, keystone, and UV/VIS co-alignment are within 0.1 pixel.

151 [2]N/S represents the North/South (cross-track) direction; E/W represents the East/West (mirror step) direction.

152 [3]Estimated with a 128 μrad E/W mirror step size (1.2 μrad overlapping between two steps) and 1181 positions.

153 [4]For the nominal mode. In the early morning or late afternoon, optimized modes can measure the daylight portion
154 every ~40 minutes. Special modes can measure a selected portion of FOR every 5–10 minutes.

155 [5]2036 out of 2048 spatial pixels are valid pixels.

156 [6]For the nominal radiance without pixel binning. It was derived using in-flight data from September 1, 2023.

157

158 ## 2.2 Signal Flow to Ground System

159 During each signal integration cycle, photons entering the slit of the TEMPO
160 spectrometer are detected at four image regions of the FPA, or more specifically, the photoactive
161 regions. Figure 2 illustrates the signal flow from the FPA to the ground system. The four image
162 regions share the same layout and are labeled quadrants A to D. Each quadrant consists of 1028
163 (spectral) × 1024 (spatial) photoactive pixels, along with four types of overclocked regions: 10
164 leading buffer columns, 22 trailing columns, 2 storage-region buffer rows, and 16 smear rows.
165 The photoactive region in each quadrant has different spectral and spatial (North-South)
166 coverage. Quadrants A and B belong to the VIS CCD, with the former covering the northern half
167 and the latter covering the southern half spatially. In the UV CCD, quadrants D and C cover the
168 northern and southern halves, respectively.

169 With the photoactive and overclocked pixels combined, each of the UV and VIS CCDs
170 has 1046 rows and 2112 columns. At the end of each integration cycle, the signals from all rows
171 in the respective CCDs are moved to the storage regions. This step is referred to as frame transfer.
172 Figure 2 shows the frame transfer direction for each CCD. Since the TEMPO CCDs are
173 shutterless, exposure still occurs during this process, resulting in smear signals added to the
174 images. The purpose of smear rows is to measure these signals.

175 The signals in the storage regions are read out to the FPE. This read-out process occurs
176 row by row, causing different rows to remain in the storage regions for different lengths of time.
177 Specifically, outer rows (e.g., those with wavelengths of ~290 or 740 nm) stay in the storage
178 regions for shorter periods than inner rows. Therefore, the dark current gained in the storage
179 regions during the entire read-out process is row-dependent. Upon uplink commands, the
180 summation of storage-region dark currents over a specific row range can be downlinked for each
181 column of each quadrant. This information is transmitted via the outermost row of the storage-
182 region buffer area in each image-region CCD quadrant.

183 In the FPE, the signals received from the storage regions are converted into digital counts
184 by 14-bit analog-to-digital converters (ADCs). Here, a conversion factor relating the number of
185 electrons to the digital counts is referred to as a gain. In practice, the gain is a weak function of
186 input signal levels, and its variation is defined as non-linearity. The ADCs of TEMPO employ
187 dual-path analog preamplifiers, where odd spatial indices take one path while even indices take
188 the other. Consequently, the odd and even spatial indices from each quadrant have different gain

values. For this reason, a set of odd or even columns from each quadrant is referred to as an octant hereafter. The digital counts obtained from each ADC contain electronic offsets, values persisting under the zero-input-signal condition. The purpose of the trailing columns in each quadrant is to measure these electronic offsets. The trailing region exhibits alternating high and low offset values between the odd and even columns within each quadrant. Therefore, the offset correction should also be performed on an octant basis. Another noteworthy characteristic of the ADCs is electronic crosstalk, which appears as mirror image ghosts between two quadrants in each of the UV and VIS CCDs.

Digital counts derived from consecutive integration cycles are co-added in the ICE. The co-adding prevents CCD wells from overfilling while ensuring that the dwell time per spatial pixel equals the product of the integration time and the number of co-adds, thereby achieving the required signal-to-noise ratio (SNR). Multiple integrations are co-added on board to establish an image at a single scan mirror position, which is then transferred to the host spacecraft for downlink to the ground system.

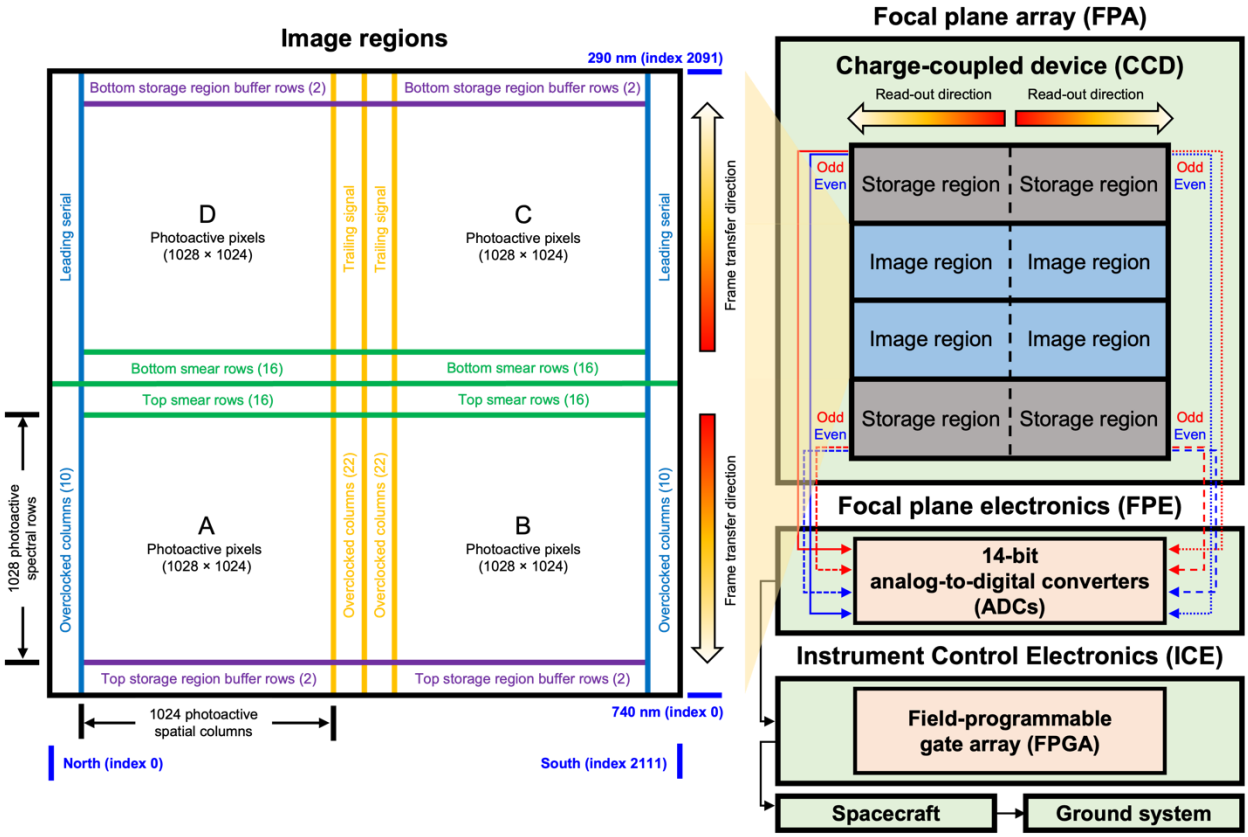

Figure 2. Signal flow from the FPA to the TEMPO ground system.

205 ### 2.3 TEMPO Operations

206 The TEMPO instrument was launched on April 7, 2023, and powered on June 7, 2023.
207 The timeframe of June 7–October 18, 2023, was defined as the commissioning period, in which
208 we conducted dry out (June 9–July 9, 2023) and cool down (July 10–12, 2023) of the instrument,
209 additional activation (e.g., scan mirror tuning and command load testing), the first-light
210 measurement of solar irradiance and Earth radiance (August 1–2, 2023), and instrument
211 characterization analyses. The nominal operations began on October 19, 2023. Here, we describe
212 essential commissioning activities and operational decisions.

213 The first dark current images were acquired the day after power on (June 8, 2023) for
214 both the image regions and storage regions of the CCDs. After additional dark current
215 measurements on five more days through July 26, 2023, we took long-duration dark current
216 measurements for the CCD image regions over 2-hour and 6-hour periods on July 28 and 30,
217 2023, respectively. These long-duration dark current measurements were used to derive a CCD
218 bad pixel map (see Section 3.1.2) and determine the relationship between the FPA temperature
219 and the dark current (see Figure 5). On August 4, 2023, we acquired dark currents with seven
220 different combinations of integration time, number of co-adds, and CCD regions (image or
221 storage). On August 18, 2023, we collected image-region dark currents while increasing the
222 integration time from 0 to 6 s. This set of measurements was used to analyze the dependence of
223 dark current derivation on integration time, electronic offset correction, and smear correction
224 (see Figure 11). One of the main purposes of image-region dark current measurements is to
225 support the removal of dark signals in solar irradiance and Earth radiance images. Beginning on
226 August 8, 2023, the nominal number of image frames has been set to 50 for dark collects
227 preceding a Sun or Earth exposure. This approach enables more reliable derivation of average
228 dark images and dynamic updates of the bad pixel map through dark current analyses across 50
229 frames.

230 The first solar irradiance measurements with the working and reference diffusers were on
231 August 1 and 2, 2023, respectively. Nominally, solar irradiance is measured with only one image
232 frame before solar midnight when the incident elevation angle onto the diffuser is 30°. Across
233 five separate days (August 12, 14, 17, 26, and 28, 2023), we took solar irradiance measurements
234 with off-nominal elevation angles with the working diffuser to analyze the goniometry
235 dependence of the measurements. Specifically, on August 17, 2023, fifteen consecutive frames

were taken instead of one nominal frame, allowing for quantifying random errors in solar irradiance (see Section 4.1.5). On September 15, 2023, we tested solar irradiance measurement post-midnight but with the nominal elevation angle. Solar measurements using the working diffuser were conducted daily through September 16, 2023, except on seven days (August 2, 5, 15, 22, 29, and September 8 and 11). Beginning with the subsequent measurement on September 21, 2023, the nominal measurement frequency was updated to once per week to slow the degradation of the working diffuser. The reference diffuser was deployed twice during the commissioning (August 2 and September 11, 2023), and its nominal measurement frequency was set to be once per three months. During nominal operations, the reference diffuser is typically deployed around each solstice and equinox, with working diffuser measurements conducted one day before and after.

The first Earth radiance measurements were on August 2, 2023. The Earth radiance measurements collected during commissioning included those specifically intended for the characterization and optimization of the scan mirror step size and the field of regard (FOR). On August 11, 2023, four different step sizes were tested (61.5, 62.5, 63.6, and 64.6 μrad) over the continent to determine the optimal nominal operation setting. Additionally, a wide range of step sizes (6.0–61.5 μrad) was tested over New York, Texas, and Los Angeles on four days (September 5, 10, 12, and 13, 2023) to achieve spatial oversampling using overlapping mirror steps. During August 18–23, 2023, we conducted optimized short scanning in the early morning or late afternoon with a 30-minute duration to cover the eastern or western half of the full FOR, the sunlit portions of the continent. The optimized scanning for the early morning and late afternoon has become a routine since August 31, 2023, but beginning on September 22, 2023, the duration and spatial coverage were updated to 40 minutes and two-thirds of the full FOR. We determined the full FOR range and scan mirror step size for nominal operation through in-flight characterization conducted on September 1, 15, 18, and 20, 2023, which tested the maximum scan mirror angles on both the North-South tilt and the East-West scan axes. The step size of 64.0 μrad was selected to cover the regional domain specified in the TEMPO FOR requirement within a 1-hour scan duration, which corresponds to 1181 mirror positions (see Table 1). Nominal 1-hour scans for the middle of the day began on September 29, 2023, over the full FOR optimized for operation. The Earth measurements during commissioning also involved other instrument characterization activities, including the acquisition of Earth radiances with three

different integration times on August 17, 2023, intended for testing signal saturation over cloudy pixels.

During commissioning, we coordinated a number of TEMPO scans with the NASA Synergistic TEMPO Air Quality Science (STAQS) and NOAA Atmospheric Emissions and Reactions Observed from Megacities to Marine Areas (AEROMMA) campaigns. Specifically, we conducted special observations over California and Arizona that involved 10-minute scanning for almost the entire day on August 23, 2023, and six 10-minute scans interleaved with hourly scans on August 27, 2023. Also, in coordination with the Coastal Texas Air Quality Observation experiment, we conducted special observations over Texas that involved 10-minute scans interleaved with hourly scans on September 11, 2023, and several hours of 10-minute scans on September 17, 19, 27, and 28, 2023. Coordination with field campaigns occurred even after commissioning. During the 2024 and 2025 Railroad Valley (RRV) vicarious calibration campaigns, the TEMPO instrument performed side slither scanning, which moves the scan mirror along the North-South tilt axis while keeping the East-West position fixed, to compare the radiometric calibration across different spatial CCD positions. Such a side-slither approach was first employed across several scans on September 19, 2023, during commissioning. Additionally, in 2025, we acquired Earth radiance measurements with high temporal sampling over certain regions for air quality analyses.

On September 25, 2023, the first twilight Earth scan was performed. Twilight measurements were collected on three consecutive days through September 27, 2023, but they were for a functional test and not paired with dark current collection preceding the Earth measurements. The first twilight radiances paired with corresponding dark current measurements were acquired during October 6–8, 2023. Twilight scans were resumed on December 22, 2023, and have been taken since for nominal operations during times that meet the instrument safety constraint (solar boresight angle > 60º) and that are not suitable for daylight radiance scanning (solar zenith angles > 80º throughout most of the FOR). Initially, these twilight scans were conducted with different exposure times from December 2023 through mid-April 2024 to optimize the measurement settings. Twilight scans are typically possible for ~8 months of the year, excluding the months centered around mid-summer, i.e., mid-April through mid-August (Carr et al., 2017).

3 Algorithm Description

The TEMPO Level 0-1 processor builds upon the heritage of existing nadir-viewing hyperspectral spectrometers, including the Global Ozone Monitoring Experiment (GOME) (Burrows et al., 1999), the Scanning Imaging Absorption Spectrometer for Atmospheric Chartography (SCIAMACHY) (Bovensmann et al., 1999), GOME-2 (Munro et al., 2016), the Ozone Monitoring Instrument (OMI) (Levelt et al., 2006), the Ozone Mapping and Profiler Suite-Nadir Mapper (OMPS-NM) (Seftor et al., 2014), the Tropospheric Monitoring Instrument (TROPOMI) (Veefkind et al., 2012), the Geostationary Trace gas and Aerosol Sensor Optimization (GeoTASO) (Leitch et al., 2014), and the Geostationary Environment Monitoring Spectrometer (GEMS) (Kim et al., 2020).

TEMPO Level 0 data have five different exposure types: dark (DRK), Earth radiance (RAD), twilight Earth radiance (RADT), working solar irradiance (IRR), and reference solar irradiance (IRRR). Key parameters associated with each exposure type are summarized in Table 2. While both RAD and RADT employ the open CMA position, they occur at different times of the day. The former is conducted during daylight for air-quality monitoring, while the latter occurs during twilight, when the Earth's disk is partially illuminated, and is only conducted when permitted by instrument safety constraints. RADT allows for the detection of city lights, nightglow, and aurora signals (Carr et al., 2025).

The TEMPO Level 0-1 processor identifies the exposure type of a given Level 0 file and processes the data through the appropriate path. Figure 3 shows a flow chart of the TEMPO Level 0-1 processor. The Version 3 processor has three main algorithm parts: (i) image processing, (ii) image navigation and registration (INR), and (iii) spectral calibration. Polarization correction has been deactivated for both RAD(T) and IRR processing in Version 3 (see the toggle signs in Figure 3), although these parts of the algorithm were already developed and integrated into the processor before TEMPO's launch. The polarization correction algorithm is currently under evaluation, and its impact on in-flight measured spectra and trace gas retrievals is being investigated. Theoretical aspects of the polarization correction are described in Appendix B.

The DRK data production is completed within image processing, while the RADT production is finished by assigning nominal geolocations after image processing. The Version 3 RAD production path encompasses image processing, INR, and spectral calibration (Figure 3).

The IRR and IRRR data undergo identical algorithm steps, including image processing and spectral calibration, but with different diffuser transmittance databases applied. The following three subsections respectively describe image processing, INR, and spectral calibration in detail. Key input and output variables for the TEMPO Level 0-1 processor are presented in Appendix A.

Table 2. Five exposure types of TEMPO.

Acronym	Description	Nominal integration time	Nominal number of co-adding	CMA position
DRK	Dark exposure	Same as the following exposure of interest (RAD, RADT, IRR, or IRRR)	Same as the following exposure of interest (RAD, RADT, IRR, or IRRR)	Closed
RAD	Geolocated Earth radiances	100 ms	26	Open
RADT	Geolocated Earth radiances (twilight)	Variable	Variable	Open
IRR	Solar irradiance	72 ms[1], 68.3 ms[2]	37[1], 40[2]	Working diffuser
IRRR	Solar irradiance (reference diffuser)	72 ms[1], 68.3 ms[2]	37[1], 40[2]	Reference diffuser

[1]Through October 4, 2024

[2]Since October 10, 2024. The change was made to avoid saturation in solar irradiance measurements.

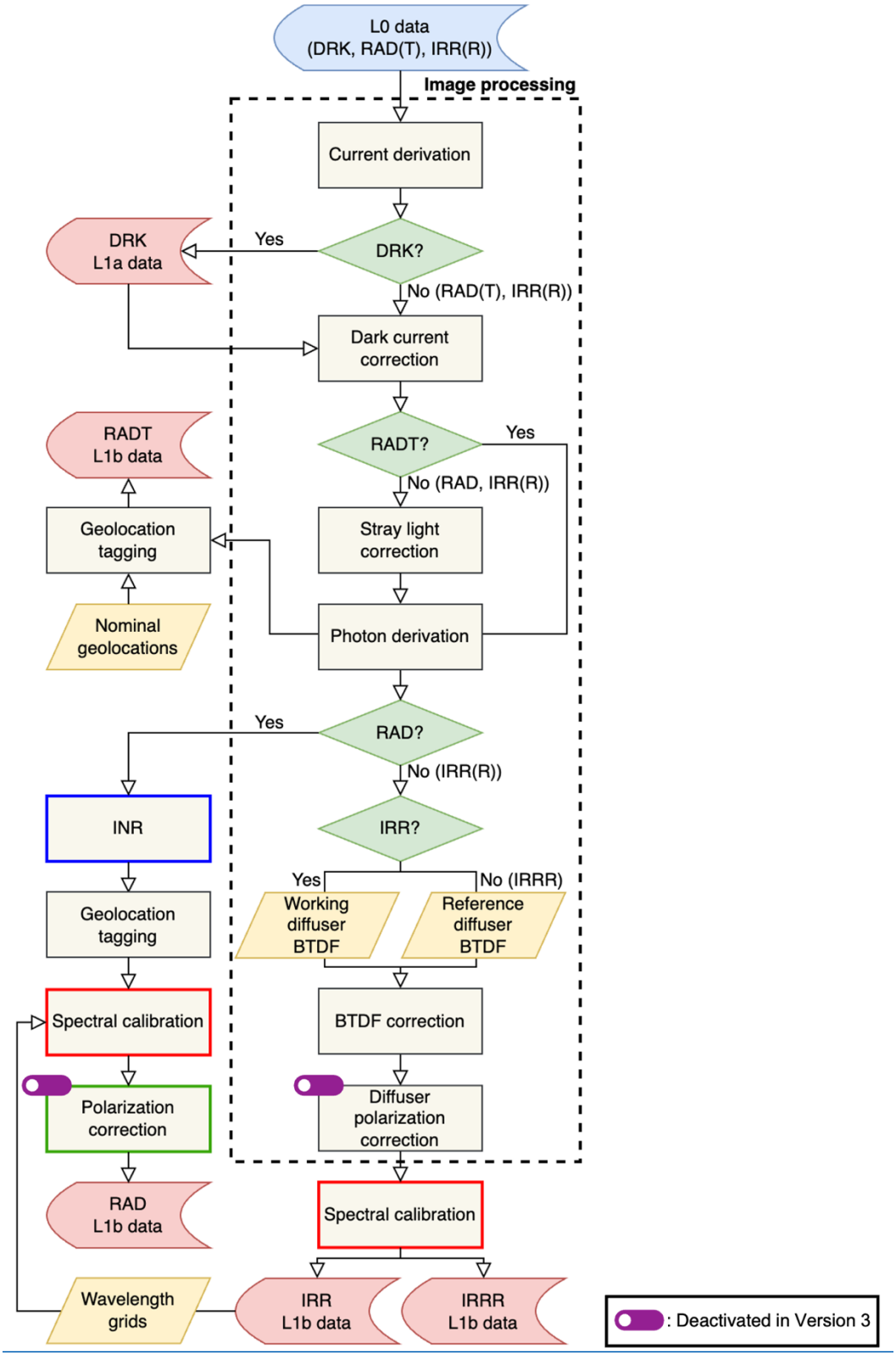

Figure 3. Flow chart of the Version 3 TEMPO Level 0-1 processor.

3.1 Image Processing

3.1.1 Forward Model

Based on the signal flow described in Section 2.2, we construct a forward model that explains the production process of the digital counts in Level 0 files. This subsection describes the forward model for different integration modes, summarized in Table 3. For integration modes 0 and 2 (Nominal and Long), integration and read-out occur in parallel, whereas for modes 1 and 3 (Short and Dark), the read-out follows integration in a sequential manner. Hence, for Earth exposure, the Short mode would take a longer total time than the Nominal mode to co-add signals to reach the same SNR level and may not be configured in practice.

Table 3. Four integration modes of TEMPO.

Name	Integer assigned	Integration time	CCD regions targeted	Corresponding exposure types
Nominal	0	100 ms	Image	RAD and DRK
Short	1	< 100 ms	Image	IRR, IRRR, and DRK
Long	2	> 100 ms	Image	RADT and DRK
Dark	3	Variable	Storage	Not applicable

The forward model accounts for the signal flow in each quadrant, first rotating it to match the orientation of quadrant A (Figure 2), then setting the indices to start from the lower-left corner. All indices in this article are 0-based unless specified otherwise. For integration modes 0–2, a signal S_{meas} measured at a photoactive CCD pixel with spectral index (row) p and spatial index (column) s in quadrant $q \in \{A, B, C, D\}$ can be modeled in units of the number of electrons as

$$S_{\text{meas}}(p,s) = [(S_{\text{use}} + \varepsilon_{\text{pol}}) + S_{\text{sl}} + S_{\text{dc}} + S_{\text{smr}} + S_{\text{sdc,read}}](p,s), \quad (1)$$

which represents the process where the useful signal S_{use} from the Earth or Sun collected for each integration cycle is combined with other signals. The term ε_{pol} denotes the change in the optical throughput signal due to the polarization of the input light. For Earth exposure, this term accounts for the response of the instrument to atmospheric polarization, whereas for Sun

365 exposure, it accounts for diffuser polarization. The term $\varepsilon_{\mathrm{pol}}$ is omitted in the subsequent
366 equations for simplicity. The term S_{sl} represents the contribution of stray light. The dark signal at
367 the photoactive CCD pixel is denoted by S_{dc}. Since S_{use}, S_{sl}, and S_{dc} correspond to signals
368 accumulated for integration time t_{int}, these terms can be expressed as follows:
369
370 $$S_{i\in\{\mathrm{use,sl,dc}\}}(p,s) = R_i(p,s) \times t_{\mathrm{int}}, \quad (2)$$
371
372 where R_i represents the signal rate of either the useful signal (R_{use}), the stray light signal (R_{sl}),
373 or the dark current (R_{dc}) in units of electrons s^{-1}. The term S_{smr} in Equation 1 indicates the
374 smear signal, which each row in a frame accumulates upon entry before integration and during
375 frame transfer after integration. Due to the frame transfer directions (Figure 2), each row
376 accumulates the smear signal as it traverses all spectral indices within each photoactive quadrant.
377 Consequently, the smear signal is constant across spectral positions within each spatial column in
378 each quadrant. The smear signal can be modeled for each quadrant as
379
380 $$S_{\mathrm{smr}}(s) = \sum_{p\in A}[R_{\mathrm{use}} + R_{\mathrm{sl}} + R_{\mathrm{dc}}](p,s) \times \frac{t_{\mathrm{ft}}}{n_A} = \frac{\sum_{p\in A}[S_{\mathrm{use}}+S_{\mathrm{sl}}+S_{\mathrm{dc}}](p,s)}{n_A} \times \frac{t_{\mathrm{ft}}}{t_{\mathrm{int}}}, \quad (3)$$
381
382 where A represents a set of the photoactive rows within the given quadrant, n_A denotes the
383 number of photoactive rows (i.e., 1028), and t_{ft} is the frame transfer time (fixed to 8.33 ms). In
384 the case of $t_{\mathrm{int}} = 0$, the smear signal is modeled as $S_{\mathrm{smr}}(s) = \sum_{p\in A} R_{\mathrm{dc}}(p,s) \times (t_{\mathrm{ft}}/n_A)$. Lastly,
385 the term $S_{\mathrm{sdc,read}}$ in Equation 1 indicates the storage-region dark signals resulting from the read-
386 out process. $S_{\mathrm{sdc,read}}$ can be estimated as
387
388 $$S_{\mathrm{sdc,read}}(p,s) = \sum_{p'=0}^{p} R_{\mathrm{sdc}}(p',s) \times \frac{t_{\mathrm{read}}}{n_Q}, \quad (4)$$
389
390 where $R_{\mathrm{sdc}}(p',s)$ is the dark current at the pixel located at (p',s) in the storage region, t_{read} is the
391 read-out time (fixed to 100 ms), and n_Q represents the number of storage-region rows per
392 quadrant (i.e., 1046).
393 In the FPE, the unit of the read-out signal S_{meas} is converted into a digital number (DN):

$$D_{\mathrm{meas}}(p,s) = S_{\mathrm{meas}}(p,s) \times g(s) + D_{\mathrm{eoff}}(p,s) + D_{\mathrm{ext}}(p,s), \quad (5)$$

where D_{meas} denotes the signal per co-add in the unit of DN, $g(s)$ represents the octant-dependent gain with a signal-dependent non-linearity effect, D_{eoff} indicates the electronic offset, and D_{ext} corresponds to the electronic crosstalk. After co-adding in the ICE, the co-added signal C_{meas} can be described by

$$C_{\mathrm{meas}}(p,s) = [D_{\mathrm{use}} + D_{\mathrm{sl}} + D_{\mathrm{dc}} + D_{\mathrm{smr}} + D_{\mathrm{sdc,read}} + D_{\mathrm{eoff}} + D_{\mathrm{ext}}](p,s) \times N_{\mathrm{co}}, \quad (6)$$

where N_{co} represents the number of co-adds, and the subscript of each digital-count term on the right-hand side represents the same as those in Equations 1 and 5. For image-region dark exposure, with $D_{\mathrm{use}} = D_{\mathrm{sl}} = 0$, Equation 6 can be simplified as

$$C_{\mathrm{meas,dc}}(p,s) = [D_{\mathrm{dc}} + D_{\mathrm{smr}} + D_{\mathrm{sdc,read}} + D_{\mathrm{eoff}} + D_{\mathrm{ext}}](p,s) \times N_{\mathrm{co}}, \quad (7)$$

where $C_{\mathrm{meas,dc}}$ represents the co-added signal from the photoactive pixel with the dark exposure setting.

In integration mode 3, with no exposure in the image regions (i.e., $D_{\mathrm{dc}} = D_{\mathrm{smr}} = 0$), the co-added signal from each storage-region pixel $C_{\mathrm{meas,sdc}}$ can be modeled as

$$C_{\mathrm{meas,sdc}}(p,s) = \left[D_{\mathrm{sdc}} + D_{\mathrm{sdc,read}} + D_{\mathrm{eoff}} + D_{\mathrm{ext}}\right](p,s) \times N_{\mathrm{co}}, \quad (8)$$

where D_{sdc} denotes the storage-region dark signal.

3.1.2 Inversion

The TEMPO Level 0-1 processor conducts an inversion of the forward model described in Section 3.1.1. The variable of ultimate interest for dark exposure (DRK) is R_{dc}, even though the contribution of $D_{\mathrm{sdc,read}}$ in Equation 7 persists throughout the process due to its inherent indistinguishability, resulting in the actual outcome of $R_{\mathrm{dc}} + S_{\mathrm{sdc,read}}/t_{\mathrm{int}}$. The processing step where the signal rates are derived in units of electrons s^{-1} is referred to as current derivation (see

Figure 1). Earth and Sun exposures (RAD, RADT, IRR, and IRRR) also share this processing step, where the outcomes are $R_{\mathrm{use}} + R_{\mathrm{sl}} + R_{\mathrm{dc}} + S_{\mathrm{sdc,read}}/t_{\mathrm{int}}$.

Issues identified during the current derivation are reported through a variable named 'pixel quality flag' in the Level 1 files. The initialization of this variable is based on a static bad pixel map, which marks CCD pixels that exhibited excessively low or high average values or standard deviations of dark current over a 2-hour period on July 28, 2023, during commissioning. Future updates may include dynamic adjustments to the bad pixel map based on the pixel-quality-flag variable derived from dark current processing.

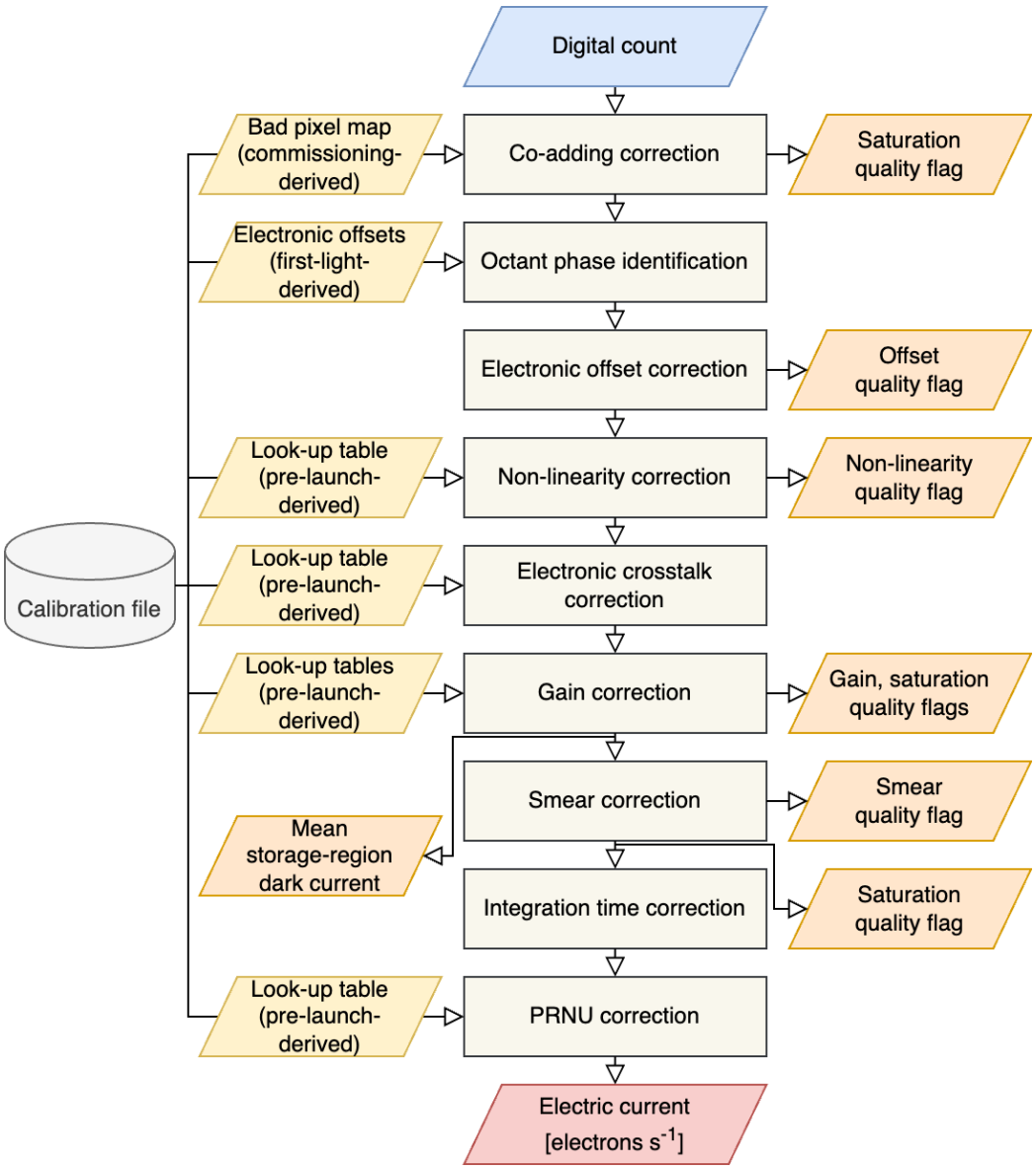

Figure 4. Flow chart of electric current derivation.

Figure 4 illustrates the correction steps included in the current derivation. The first step is co-adding correction, which corresponds to an inversion from Equation 6 to Equation 5. Here, the signal per co-add D_{meas} is calculated in the unit of DN:

$$D_{\mathrm{meas}}(p,s) = \frac{C_{\mathrm{meas}}(p,s)}{N_{\mathrm{co}}}. \quad (9)$$

At this step, the algorithm examines two types of saturations: (i) read-out saturation and (ii) co-add saturation. The former occurs if the input signal from a single read-out exceeds the maximum value the 14-bit ADCs can represent, after accounting for the electronic offset. The latter occurs if the signal co-added in the ICE exceeds the maximum value allowed by the 20-bit digital resolution (i.e., $2^{20} - 1$ DN). However, saturation caused solely by co-adding is practically impossible because the flight software uses a 6-bit register to set the number of co-adds. If there are any saturated pixels, their locations are marked in the pixel-quality-flag variable.

The following step is octant phase identification, which determines the ADC path and assigns the appropriate pre-launch gain value for each octant. This step begins with the gain pre-assigned to each octant. Section 4.1.1 provides a description of the pre-assignment. To determine whether the ADC paths have changed, the Level 0-1 processor compares the offsets between odd and even trailing columns on a frame-by-frame basis, since the two ADC paths produce different offset levels (see Section 2.2). If a parity change is detected, the gain values for the two octants are automatically switched and reassigned.

The third step of current derivation is electronic offset correction. There are two major approaches for offset correction, depending on how to determine offset values for each octant: (i) a constant offset derived using signals from the intersection of the trailing and smear areas (see Figure 2) and (ii) row-by-row offsets derived using signals from all trailing rows. The Version 3 Level 0-1 processor employs the latter for frame-by-frame offset correction. Section 4.1.2 explains the rationale behind this implementation. The offset correction can be represented by

$$D^{\mathrm{eoff}}_{\mathrm{meas}}(p,s) = D_{\mathrm{meas}}(p,s) - D_{\mathrm{eoff}}(p,s), \quad (10)$$

where $D^{\mathrm{eoff}}_{\mathrm{meas}}(p,s)$ denotes the offset-corrected signal in the unit of DN. If a negative value is obtained as a result of the correction, the pixel location is marked via the pixel-quality-flag variable.

Electronic offset correction is followed by non-linearity correction. This step employs a pre-launch look-up table that provides a corrected digital count for every integer from 0 to 16,383 (i.e., $2^{14} - 1$) for each octant:

$$D^{\mathrm{nl}}_{\mathrm{meas}}(p,s) = L(D^{\mathrm{eoff}}_{\mathrm{meas}}(p,s)), \tag{11}$$

where L denotes the look-up table function, involving a linear interpolation between neighboring nodes, and $D^{\mathrm{nl}}_{\mathrm{meas}}(p,s)$ represents the non-linearity-corrected signal. If a negative value results from the correction, the corresponding pixel location is reported via the quality flag.

The following step is electronic crosstalk correction, described by

$$D^{\mathrm{ext}}_{\mathrm{meas}}(p,s) = D^{\mathrm{nl}}_{\mathrm{meas}}(p,s) - D_{\mathrm{ext}}(p,s), \tag{12}$$

where $D^{\mathrm{ext}}_{\mathrm{meas}}$ represents the crosstalk-corrected signal. The processor estimates D_{ext} as the product of the signal from the spatially mirrored position and the corresponding crosstalk coefficient obtained from a pre-launch look-up table, with a typical value of ~0.0015.

Gain correction converts the crosstalk-corrected digital counts into the number of electrons:

$$S'_{\mathrm{meas}}(p,s) = \frac{D^{\mathrm{ext}}_{\mathrm{meas}}(p,s)}{g_0(s)}, \tag{13}$$

where $g_0(s)$ represents the octant-dependent gain, corrected for the dependence on FPE temperature. Note that $g_0(s)$ is distinguished from the gain in Equation 5, $g(s)$, by the added subscript, reflecting that non-linearity correction is performed directly on the digital counts in a separate step (see Equation 11). The resulting number of electrons $S'_{\mathrm{meas}}(p,s)$ is distinguished from $S_{\mathrm{meas}}(p,s)$ by notation, considering the photo response non-uniformity (PRNU) correction is not yet performed.

After gain correction, the processor verifies whether the number of electrons exceeds the effective CCD well (i.e., the serial read-out saturation limit, which is 270,040). If detected, saturation is reported via the quality flag. Additionally, any negative values resulting from the gain correction are marked in the pixel-quality-flag variable.

Then, the processor calculates the mean storage-region dark signal for each quadrant. The primary purpose is to use the corresponding output for dark current correction, which is a processing step following current derivation (see Figure 3). As described in Section 2.2, each column of the outermost row p_f in quadrant q provides a summation of storage-region dark signals over a certain range of rows, determined by uplink commands (rows 99–999, in Version 3). Using S'_{meas} from row p_f, the mean storage-region dark signal $\overline{S_{\mathrm{sdc}}}$ is calculated:

$$\overline{S_{\mathrm{sdc}}}(q) = \frac{\sum_{s \in G} S'_{\mathrm{meas}}(p_f(q), s)}{N_G} \times \frac{1}{N_{\mathrm{tg}}}. \tag{14}$$

The calculation involves only "good" CCD pixels, with no issues reported via the pixel-quality-flag variable from the preceding steps. The variables G and N_G in Equation 14 indicate the subset of good CCD pixels in row $p_f(q)$ and the number of those good pixels. The variable N_{tg} represents the number of storage-region rows aggregated at row $p_f(q)$.

The $\overline{S_{\mathrm{sdc}}}$ calculation is followed by the estimation of uncertainties in the useful signals for the photoactive regions:

$$\varepsilon_S^2(p, s) = S'_{\mathrm{meas}}(p, s) + \varepsilon_{\mathrm{CTE}}^2(p, s) + \varepsilon_{\mathrm{read}}^2 + \varepsilon_{\mathrm{quan}}^2, \tag{15}$$

where ε_S represents the estimated signal uncertainty, and $\varepsilon_{\mathrm{CTE}}$, $\varepsilon_{\mathrm{read}}$, and $\varepsilon_{\mathrm{quan}}$ denote the charge-transfer-efficiency (CTE) noise, read-out noise, and quantization noise, respectively. The CTE of the TEMPO CCDs is 0.99997, i.e., approximately three photoelectrons are lost for every 100,000 shifts during charge transfer, introducing noise in measurements. The read-out noise ($\varepsilon_{\mathrm{read}}$) occurs in the amplifiers while converting the charges to voltages. The quantization noise ($\varepsilon_{\mathrm{quan}}$) is generated during the conversion of the voltages to digital counts.

Smear signals are then removed from the derived number of electrons:

$$S'^{\mathrm{smr}}_{\mathrm{meas}}(p,s) = S'_{\mathrm{meas}}(p,s) - S_{\mathrm{smr}}(p,s), \quad (16)$$

where $S'^{\mathrm{smr}}_{\mathrm{meas}}(p,s)$ represents the smear-corrected signal. There are two major approaches to estimating smear signals. The first is to use the signals measured at the overclocked smear rows in the CCDs (see Figure 2), and the second is to multiply the signals from the photoactive regions by the ratio between the frame transfer time and the integration time (see Equation 3). We refer to the first and second as the overclock method and time-based scaling, respectively. Based on an analysis using in-flight dark current measurements, the Version 3 Level 0-1 processor employs the time-based scaling method (see Section 4.1.3).

After smear correction, neighbors of saturated pixels are masked, considering the potential transfer of excess charge from the saturated pixels to adjacent ones. If the number of electrons exceeds 360,000 at a given photoactive pixel, "charge blooming" occurs in both directions along the spectral CCD dimension, confined to the corresponding spatial column, before frame transfer. Subsequently, the charge spreads in the spatial dimension during read-out if the number of electrons exceeds the effective CCD well (270,040), but only to the next pixel in the read-out order (see Figure 2). To be conservative, the neighbors of saturated pixels are also masked as saturated in the pixel-quality-flag variable. In Version 3, the neighbors are defined as pixels within ±2 spectral indices and ±1 spatial indices of each saturated pixel.

Then, the Level 0-1 processor divides the derived number of electrons by integration time in the photoactive regions (or, simply, active regions). This step is referred to as integration time correction:

$$R'^{\mathrm{smr}}_{\mathrm{meas}}(p,s) = \frac{S'^{\mathrm{smr}}_{\mathrm{meas}}(p,s)}{t_{\mathrm{int}}}, \quad (17)$$

where $R'^{\mathrm{smr}}_{\mathrm{meas}}(p,s)$ denotes the resulting electric current in the unit of electrons s^{-1}. The signal uncertainty ε_S is also divided by integration time to derive the corresponding electric current uncertainty ε_R:

$$\varepsilon_R(p,s) = \frac{\varepsilon_S(p,s)}{t_{\mathrm{int}}}. \quad (18)$$

Additionally, the mean storage-dark signal $\overline{S_{\mathrm{sdc}}}$ for each quadrant (q) is converted into current $\overline{R_{\mathrm{sdc}}}$ using t_{read}:

$$\overline{R_{\mathrm{sdc}}}(q) = \frac{\overline{S_{\mathrm{sdc}}}(q)}{t_{\mathrm{read}}} \times \frac{n_Q}{p_{\mathrm{sdc,cen}}}. \tag{19}$$

As the storage-region dark signal varies depending on the duration the row remains before read-out, the equation incorporates $p_{\mathrm{sdc,cen}}$ and n_Q, which represent the index of the aggregated rows' center and the number of storage-region rows per quadrant (i.e., 1046), respectively.

Integration time correction is followed by the correction of PRNU, which represents pixel-to-pixel response variation characterized using flat-field illumination before launch:

$$R^{\mathrm{smr}}_{\mathrm{meas}}(p,s) = \frac{R'^{\mathrm{smr}}_{\mathrm{meas}}(p,s)}{P(p,s)}, \tag{20}$$

where $P(p,s)$ represents the PRNU obtained from the pre-launch look-up table. As a result of PRNU correction, which is the last step of the current derivation, the electric current $R^{\mathrm{smr}}_{\mathrm{meas}}$ (i.e., $(S_{\mathrm{meas}} - S_{\mathrm{smr}})/t_{\mathrm{int}}$) is derived for each CCD pixel.

The DRK processing ends with the current derivation, and a corresponding Level 1a file is generated (see Figure 3). For the other exposure types, the following processing step is dark current correction. One important aspect of this correction is that dark current is variable and is unable to be measured simultaneously with solar irradiance or Earth radiance. Therefore, we need to estimate R_{dc} using the most recent DRK data available at the time of dark current correction. The estimated dark current is subtracted from the derived electric current:

$$R^{\mathrm{illum}}_{\mathrm{meas}}(p,s) = \left[R^{\mathrm{smr}}_{\mathrm{meas}} - R^{\mathrm{smr}}_{\mathrm{meas,dc}}\right](p,s) = R^{\mathrm{smr}}_{\mathrm{meas}}(p,s) - \left[R_{\mathrm{dc}} + \left(\frac{S_{\mathrm{sdc,read}}}{t_{\mathrm{int}}}\right)\right](p,s). \tag{21}$$

Here, $R^{\mathrm{smr}}_{\mathrm{meas,dc}}(p,s)$ and $R^{\mathrm{illum}}_{\mathrm{meas}}(p,s)$ indicate the estimated dark current and the dark-current-corrected electric current, respectively. The former is derived using the most recently measured dark current under the same co-adding and integration time conditions as $R^{\mathrm{smr}}_{\mathrm{meas}}$. Note that the measured dark current inherently contains storage-region dark current from read-out, which

offers here simultaneous removal of the active-region (R_{dc}) and storage-region ($S_{\mathrm{sdc,read}}/t_{\mathrm{int}}$) dark current. If a negative value occurs as a result of subtraction, it is reported via the pixel-quality-flag variable.

Since dark current is a function of FPA temperature, we refer to the estimation of dark current at this stage as temperature correction. There are two major approaches for the temperature correction of dark current: the one using FPA temperature and the other using storage-region dark current. Figure 5 shows temporal variations across 183 frames of mean active-region dark current, along with the corresponding storage-region dark current and FPA temperature, observed with a DRK exposure on July 28, 2023. Here, the mean active-region dark current represents the per-quadrant averages of $R^{\mathrm{smr}}_{\mathrm{meas,dc}}$, while the mean storage-region dark current represents $\overline{R_{\mathrm{sdc}}}$ calculated using Equation 19. The FPA temperature refers specifically to the temperature measured at the FPA strap. The three variables exhibit strong correlations with one another, confirming that the FPA temperature drives the CCD dark current response.

Nominally, each DRK exposure contains 50 frames of active-region dark current. The processor calculates the average $R^{\mathrm{smr}}_{\mathrm{meas,dc}}$ and $\overline{R_{\mathrm{sdc}}}$ for each CCD pixel over these frames, as well as the average FPA temperature. When using the FPA-temperature option, the temperature correction is performed by

$$R^{\mathrm{smr}}_{\mathrm{meas,dc}}(p,s) = \left\{R^{\mathrm{smr},T0}_{\mathrm{meas,dc}} \times \exp\left[a \times \left(\frac{1}{T} - \frac{1}{T_0}\right)\right]\right\}(p,s), \tag{22}$$

where T indicates the FPA temperature at the time of Earth or Sun exposure, while T_0 and $R^{\mathrm{smr},T0}_{\mathrm{meas,dc}}$ represent the average FPA temperature during the dark exposure and the corresponding average dark current measurement. The coefficient a determines the relationship between dark current and FPA temperature. On the other hand, the storage-region-based temperature correction is expressed as

$$R^{\mathrm{smr}}_{\mathrm{meas,dc}}(p,s) = R^{\mathrm{smr},T0}_{\mathrm{meas,dc}} \times \frac{\overline{R_{\mathrm{sdc}}}}{\overline{R^{T0}_{\mathrm{sdc}}}}, \tag{23}$$

where $\overline{R_{\mathrm{sdc}}^{T0}}$ represents the frame-averaged mean storage-region dark current during the dark exposure. In this approach, we assume that the active and storage regions respond equivalently to FPA temperature variations.

We recently noted the possibility that measurements from rows p_f may contain additional signals mixed with the storage-region dark, particularly with the Version 3 configuration. Although this contamination has a negligible impact on DRK/RADT, it exerts a more pronounced effect on RAD/IRR(R) due to differences in signal levels. Therefore, the Version 3 Level 0-1 processor employs Equations 23 and 22 to perform dark current correction for RADT and RAD/IRR(R), respectively. Further investigations into the storage region will be conducted.

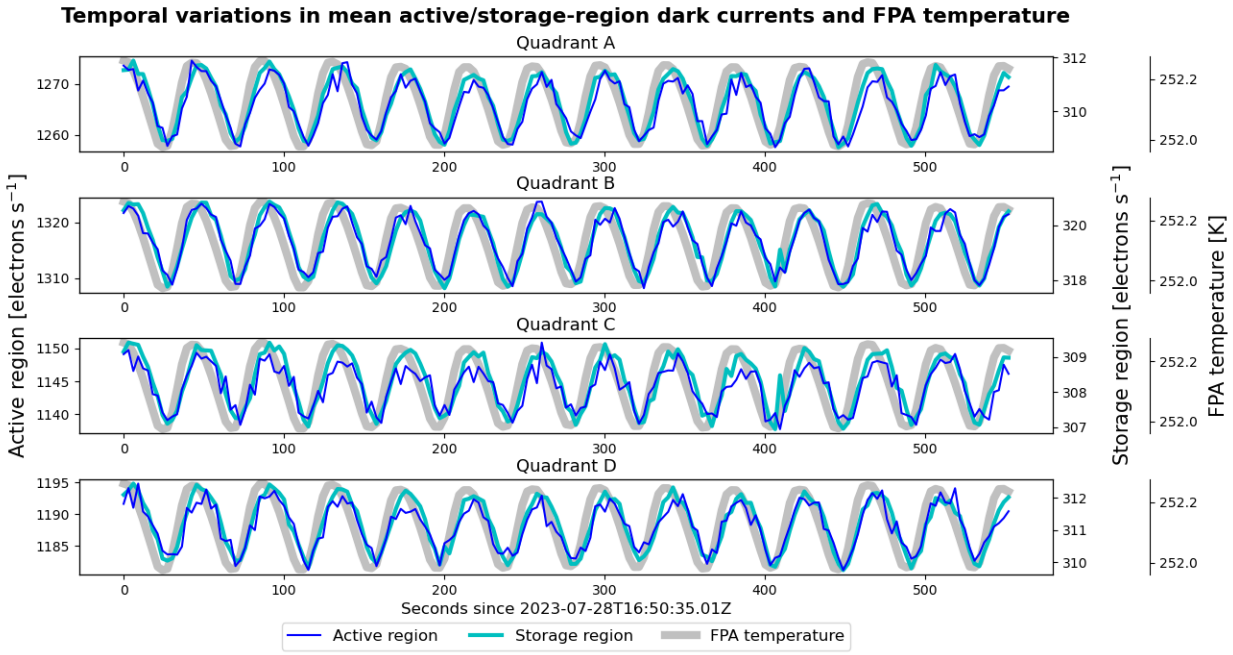

Figure 5. Temporal variations in mean active- and storage-region dark currents and FPA temperature, observed with DRK exposure on July 28, 2023.

For the RAD and IRR(R) processing, dark current correction is followed by stray light correction (see Figure 3). The RADT processing skips this step, considering low signals detected during twilight hours. The TEMPO stray-light correction algorithm employs pre-launch point spread functions (PSFs). Figure 6a shows an example of PSF, derived with illumination targeting spatial index 1023 (the center) at 390 nm wavelength. This panel demonstrates that stray light

has 2-dimensional impacts on the CCDs; however, the magnitudes are significantly smaller in the spatial dimension. Besides, from an operational perspective, it is time-consuming to account for 2-dimensional stray light. Therefore, we consider only spectral stray light:

$$R_{\mathrm{meas}}^{\mathrm{illum}}(p,s) = R_{\mathrm{meas}}^{\mathrm{ib}}(p,s) + \sum_{m=0}^{2055}(d_{p,m} \times R_{\mathrm{meas}}^{\mathrm{ib}}(m,s)), \quad (24)$$

where $d_{p,m}$ represents the PSF element accounting for the stray light influence from row m on row p, and $R_{\mathrm{meas}}^{\mathrm{ib}}$ represents the in-band or stray-light-corrected current (Zong et al., 2007). Equation 24 can be converted into matrix form:

$$\boldsymbol{R}_{\mathrm{meas}}^{\mathrm{illum}} = [\boldsymbol{I} + \boldsymbol{D}] \cdot \boldsymbol{R}_{\mathrm{meas}}^{\mathrm{ib}} = \boldsymbol{A} \cdot \boldsymbol{R}_{\mathrm{meas}}^{\mathrm{ib}}, \quad (25)$$

where $\boldsymbol{R}_{\mathrm{meas}}^{\mathrm{illum}}$ and $\boldsymbol{R}_{\mathrm{meas}}^{\mathrm{ib}}$ are 2-dimensional matrices representing $R_{\mathrm{meas}}^{\mathrm{illum}}$ and $R_{\mathrm{meas}}^{\mathrm{ib}}$, and $\boldsymbol{D}$ is a matrix with dimensions of 2056 × 2056 constituted with the 1-dimensional PSFs. Figure 6b shows the matrix $\boldsymbol{D}$ constructed using the TEMPO 1-dimensional PSFs, while Figure 6c presents several rows of the matrix $\boldsymbol{D}$. The matrix $\boldsymbol{A}$ is defined by the sum of $\boldsymbol{D}$ and the identity matrix $\boldsymbol{I}$. The stray-light-corrected currents can be derived by the inversion:

$$\boldsymbol{R}_{\mathrm{meas}}^{\mathrm{ib}} = \boldsymbol{A}^{-1} \cdot \boldsymbol{R}_{\mathrm{meas}}^{\mathrm{illum}}, \quad (26)$$

which can also be expressed in scalar form:

$$R_{\mathrm{meas}}^{\mathrm{ib}}(p,s) = R_{\mathrm{meas}}^{\mathrm{illum}}(p,s) - R_{\mathrm{sl}}(p,s), \quad (27)$$

where $R_{\mathrm{sl}}(p,s)$ indicates the stray light current. If stray light correction results in negative values, those pixels are marked in the pixel-quality-flag variable.

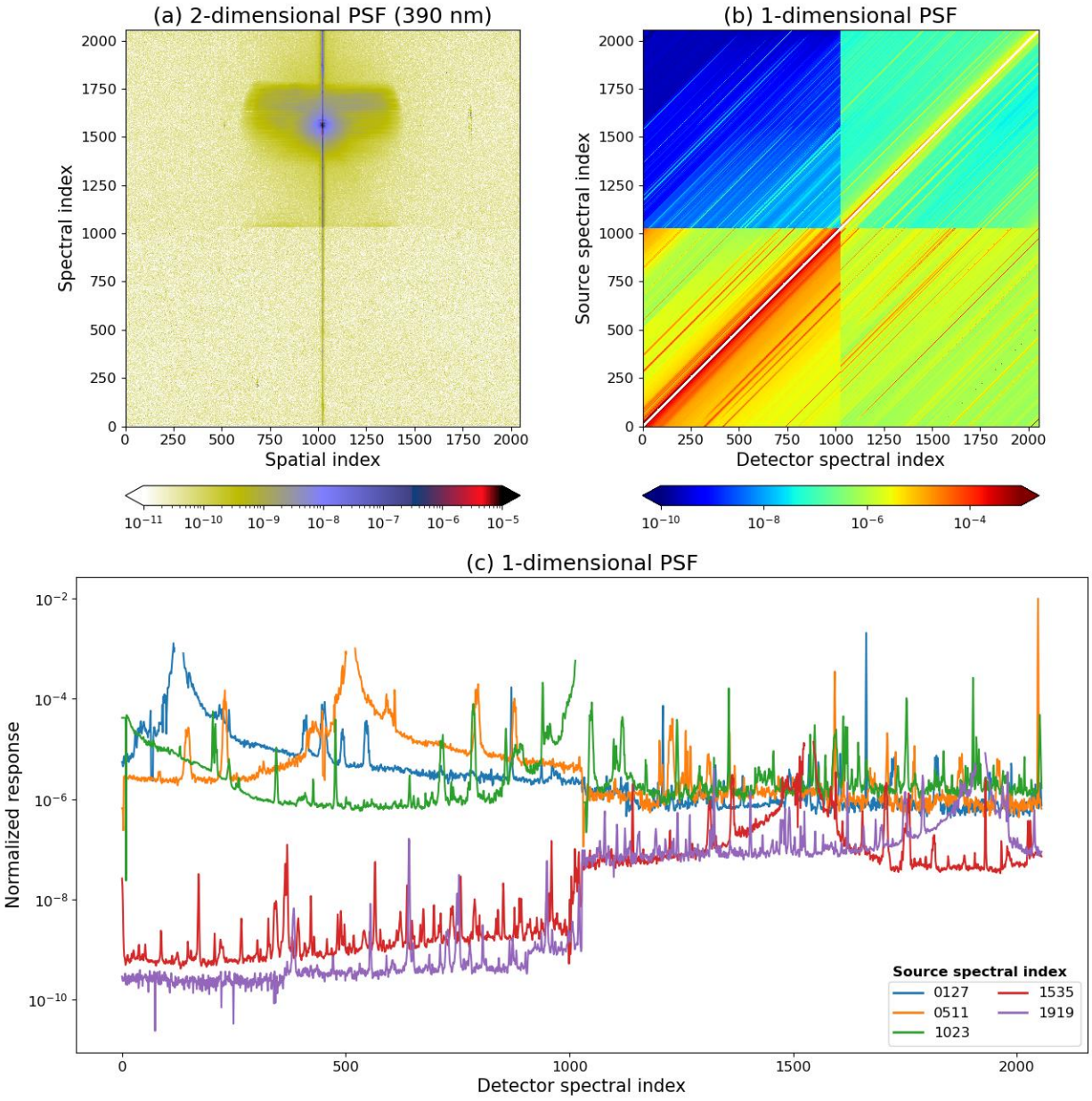

Figure 6. TEMPO stray-light PSFs. (a) An example of 2-dimensional PSF, derived pre-launch with illumination targeting spatial index 1023 (the center) at 390 nm wavelength; (b) the matrix ***D*** constructed using the TEMPO 1-dimensional PSFs. See text for the definition of the matrix ***D***; (c) examples of rows of the matrix ***D***. The selected row indices are shown in the legend inset.

664 The following processing step is photon derivation, which concerns all four exposure
665 types except DRK (see Figure 3). In this step, pre-launch radiometric calibration coefficients
666 $K(p,s)$ are multiplied by the currents to convert the units:
667
668 $$I^{\mathrm{ib}}_{\mathrm{meas}}(p,s) = R^{\mathrm{ib}}_{\mathrm{meas}}(p,s) \times K(p,s), \quad (28)$$
669
670 where $I^{\mathrm{ib}}_{\mathrm{meas}}$ represents Earth radiance (RAD and RADT) or pre-diffuser-corrected solar
671 measurement (IRR and IRRR) in the unit of photons s^{-1} cm^{-2} nm^{-1} sr^{-1}. The radiometric
672 calibration coefficients are also multiplied by the electric current uncertainty (ε_R) derived in
673 Equation 18 to derive the radiance or irradiance uncertainty $\varepsilon_{\mathrm{meas}}$ with the consistent unit:
674
675 $$\varepsilon_{\mathrm{meas}}(p,s) = \varepsilon_R(p,s) \times K(p,s). \quad (29)$$
676
677 Analyses of $\varepsilon_{\mathrm{meas}}$ estimated using in-flight measurements are presented in Section 4.1.5.
678 After photon derivation, the RAD processing continues to INR (see Figure 3), which is to
679 be described in Section 3.2. On the other hand, the RADT image processing ends here (note that
680 RADT radiances are derived using $I^{\mathrm{illum}}_{\mathrm{meas}}(p,s) = R^{\mathrm{illum}}_{\mathrm{meas}}(p,s) \times K(p,s)$, rather than Equation 28,
681 since stray light correction is not applied). Instead of undergoing the INR step, the RADT Level
682 1b files are generated by applying nominal geolocations, followed by geolocation tagging that
683 assigns land cover information, terrain height, and viewing and solar geometries to each ground
684 pixel. Details of the geolocation tagging are described in Section 3.2.
685 The IRR and IRRR types remain in the image processing because, unlike Earth exposure,
686 they deploy diffusers for measurements. The working diffuser and the reference diffuser exhibit
687 different transmittances, which are characterized by the bidirectional transmittance distribution
688 functions (BTDFs). The processor corrects solar irradiance values obtained from Equation 28,
689 accounting for the BTDF at every photoactive CCD pixel. This step is referred to as BTDF
690 correction. The two diffusers employ different pre-launch BTDF look-up tables in this process
691 (see Figure 3).
692 Figure 7 shows the goniometry of the diffuser transmission. The transmittances vary
693 depending on wavelength and goniometric conditions, and the corresponding information is
694 stored in pre-launch look-up tables. Before the TEMPO launch, the elevation angle of the

incident light was specifically expected to be the primary factor governing the transmittances. However, during the commissioning phase after launch, we noticed that the transmittances are better characterized considering the scattering angle (see Figure 7), leading to a change in the BTDF correction method (Section 4.1.4). The updated correction is applied as follows:

$$\tau(\lambda, s) = \tau_{\mathrm{LUT}}(\lambda, s) \times (1 + e) \times \frac{1}{1+e'} \times \frac{1}{1+s\prime(\lambda,s)}, \quad (30)$$

where $\tau_{\mathrm{LUT}}(\lambda, s)$ and $\tau(\lambda, s)$ represent the look-up-table and goniometry-corrected transmittance values in the unit of sr^{-1}, respectively, with λ indicating wavelength. The variable e indicates the elevation angle correction:

$$e = (c_1 \times \lambda + c_2) \times \frac{(\theta - \theta_{\mathrm{nom}})}{100}, \quad (31)$$

where θ_{nom} and θ are the nominal elevation angle (30°) and the elevation angle at the time of measurement, respectively. The coefficients c_1 and c_2 are obtained from the look-up table. The variable e' in Equation 30 represents an extra elevation angle correction derived using fifteen consecutive frames of solar irradiance taken on August 17, 2023:

$$e' = (c'_1 \times \lambda + c'_2) \times \frac{(\theta_{\mathrm{nom}} - \theta)}{100}, \quad (32)$$

with the corresponding coefficients c'_1 and c'_2. The variable s' in Equation 30 indicates the scattering angle correction:

$$s'(\lambda, s) = -f \times (c_1 \times \lambda + c_2) \times \frac{[\gamma(\lambda,s) - \gamma_{\mathrm{nom}}(\lambda,s)]}{100}, \quad (33)$$

where f is a correction factor for $c_1$and c_2, accounting for the difference between pre-launch and in-flight characteristics. The variables γ_{nom} and γ represent the nominal scattering angle and the scattering angle at the time of measurement, respectively.

After deriving the goniometry-corrected transmittance $\tau(\lambda, s)$, the BTDF correction is performed by

$$I_{\text{meas}}^{\text{ib,t}}(p,s) = \frac{I_{\text{meas}}^{\text{ib}}(p,s)}{\tau(\lambda(p,s),s)} \times k(s), \tag{34}$$

where $I_{\text{meas}}^{\text{ib,t}}(p,s)$ represents the BTDF-corrected solar irradiance in the unit of photons s^{-1} cm^{-2} nm^{-1}. Here, $k(s)$ represents a trend parameter set to unity at launch, with plans for updating it through comparisons between solar irradiances measured using the working and reference diffusers.

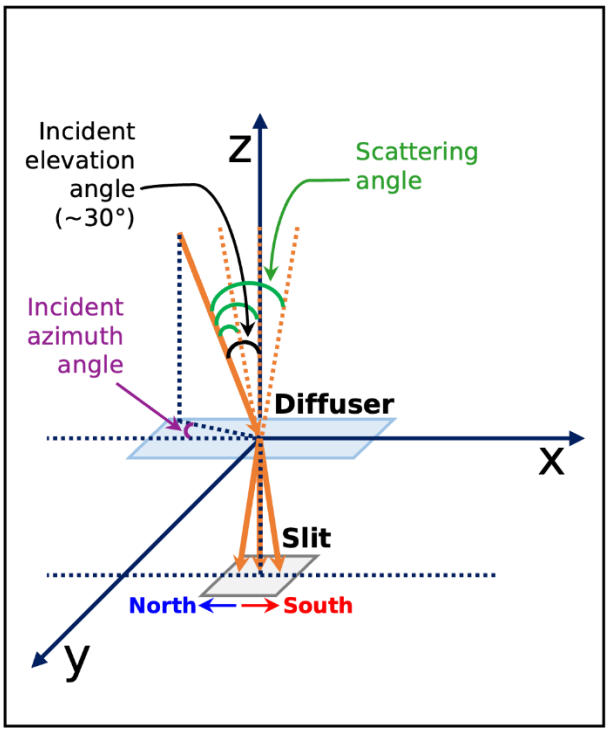

Figure 7. Schematic diagram for the geometry of the diffuser transmission.

To summarize, the final outputs of the Version 3 image processing for RADT, RAD, and IRR(R) correspond to $I_{\text{meas}}^{\text{illum}}$, $I_{\text{meas}}^{\text{ib}}$, and $I_{\text{meas}}^{\text{ib,t}}$, respectively, each resulting from a different processing stage. All three outputs are regarded as the useful (ir)radiance I_{use}, although uncorrected terms in the Level 0 data (Equations 1 and 6) may introduce uncertainty. Ideally, accurate polarization correction can enhance the performance of the RAD and IRR(R) processing

(Appendix B). Algorithm testing for polarization correction using in-flight measurements will be addressed in a future study.

3.2 Image Navigation and Registration (INR)

After the image processing for the RAD product, INR takes place (see Figure 3). INR is implemented both in space and on the ground. The primary purpose of INR processing is to add geographic coordinates to each spatial pixel in the Level 1 granules. The definition of these coordinates is illustrated in Figure 8b. A pixel might contain an object that is either on the ground or at some altitude above it, such as clouds. The Version 3 INR processing first determines the object's location as it appears in WGS-84 ellipsoid coordinates from the vantage point of TEMPO (lon0, lat0). This is completely analogous to the definition of pixel locations in the Advanced Baseline Imager (ABI) "fixed grid" for the Geostationary Operational Environmental Satellites–R series (GOES-R) (Kalluri et al., 2018). Then, the INR processing corrects for terrain parallax to provide the object's location in the terrain-registered coordinates (lon, lat, h).

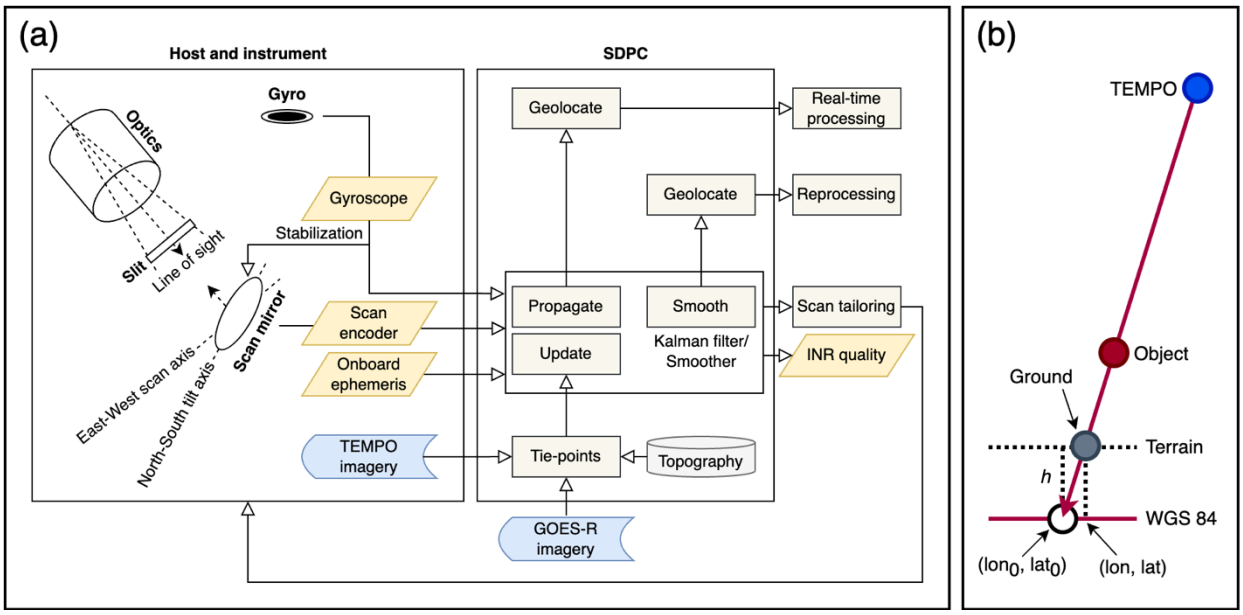

Figure 8. Schematic diagram for INR processing. Panel (a) shows a flow chart of the TEMPO INR processing, and panel (b) illustrates the definition of geographic coordinates.

761 Figure 8a shows the INR processing for TEMPO in detail (Carr, 2016). The host
762 spacecraft provides knowledge of its location in orbit as determined by an onboard Global
763 Navigation Satellite System (GNSS) receiver with an uploaded ephemeris as a backup. The host
764 also provides body rates that are used for ground INR processing and stabilizing the pointing of
765 the TEMPO scan mirror. Scan encoders provide the ground processing with the orientation of the
766 scan mirror.
767 Ground INR processing forms blue and red images of the Earth by weighting the TEMPO
768 spectral planes so that they have an equivalent spectral response to ABI bands 1 (blue) and 2
769 (red). The TEMPO blue and red images are formed using UV and VIS radiances, respectively.
770 Pointing truth is provided by tie-points (template matching) between the TEMPO blue (red)
771 images and ABI band 1 (2). ABI imagery is known to be very accurately geolocated (Tan et al.,
772 2018) and, therefore, a good source of pointing truth. The tie-point templates can represent
773 terrain under clear skies, partially cloudy, or fully cloudy conditions. Binocular tie points are
774 preferentially used. These tie-points are where the same pattern from TEMPO is matched to ABI
775 imagery from both the East and West GOES-R satellites. Binocular tie-points provide the
776 ellipsoid location of the pattern and its height above the ellipsoid, which is possible because of
777 the depth perception of binocular vision. Monocular tie points are used when the coverage by the
778 two GOES-R satellites does not overlap. Monocular tie points assume a nominal altitude above
779 the terrain, and they have additional errors in the direction of the parallax shift because of the
780 uncertainty of the feature altitude in the template.
781 Tie-point measurements are consumed by a Kalman Filter, which has a geometric model
782 that represents the geometric optical process of TEMPO forming an image of a spatial pixel. It
783 represents the unknowns in this model as a state vector, including orientation of TEMPO, orbit
784 of the host, magnification, spatial smile, and scan scale-factor and linearity corrections. The state
785 vector updates after each tie-point and each ephemeris update. The state vector is propagated
786 from one tie-point to another using simple orbital dynamics and the gyroscope body rates. The
787 estimated states provide a prompt determination of the pixel geographic coordinates; however,
788 smoothing improves the states and geographic coordinates. The Smoother is run at the
789 completion of the scan. It starts with the last granule and works backward to the first. The
790 Smoother effectively propagates information from the future backward to improve knowledge of
791 the present and thereby reduce the transient response of the system. The smoothed states are used

for the final navigation of each granule before handing it off to the next processing steps. The Kalman Filter also outputs tie-point residuals and model covariances that are indicative of INR performance. Predicted scan-center offsets are also output and used to tailor the scan locations so that they efficiently cover their intended targets.

The geographic assignments for the RADT product are nominal, based on the ephemeris and continuous integration of the body rate telemeter. More accurate geographic assignments can be made in post-processing using Day/Night Band (DNB) nighttime imagery from the Visible Infrared Imaging Radiometer Suite (VIIRS) instrument as pointing truth (Carr et al., 2025).

Once geolocations are assigned either to the RAD or RADT product, the Level 0-1 processor associates each ground pixel with ancillary information through geolocation tagging (see Figure 3). First, the algorithm calculates the fraction of pixel area covered by snow or ice. The snow and ice cover information is obtained from daily NOAA/NESDIS Interactive Multisensor Snow and Ice Mapping System (IMS) Version 1.3 data with 1-km resolution (U.S. National Ice Center, 2008). The second step is terrain height calculation. The algorithm employs the Global Multi-resolution Terrain Elevation Data 2010 (GMTED2010) at 30″ resolution (Danielson and Gesch, 2011) and derives an area-weighted terrain height for each TEMPO ground pixel. Then, four observation geometry angles are calculated for the center of each pixel: the zenith and azimuth angles for both the viewing and solar directions. Lastly, the algorithm assigns the land cover type to each TEMPO pixel using the Moderate Resolution Imaging Spectroradiometer (MODIS) Land Cover Type Product (MCD12Q1) Version 5 (Friedl et al., 2010) through nearest-neighbor lookup and determines whether each pixel is under sun glint or solar eclipse conditions.

3.3 Spectral Calibration

The final processing step for the RAD, IRR, and IRRR products is spectral calibration (see Figure 3). The spectral calibration algorithm determines the wavelength grid for a given measurement spectrum via cross-correlation with a reference spectrum (Chance, 1998). This section provides only a brief introduction to the online spectral calibration as part of the TEMPO Level 0-1 processor. A more detailed algorithm description and spectral performance of TEMPO can be found in a companion paper (Hou et al., 2025).

The online spectral calibration process specifically targets the entire spectral coverage of each CCD (UV and VIS) separately. Running the algorithm involves three main determinations: (i) initializing the wavelength grid for the measurement, (ii) selecting the reference spectrum, and (iii) composing the state vector for spectral fitting. The RAD and IRR(R) processing employs different configurations for those three while sharing the same algorithm structure. The primary reason for the differences is that the computational cost is significantly higher to perform spectral calibration on Earth spectra for each mirror step.

Figure 9 displays a flow chart of the TEMPO spectral calibration algorithm. The IRR(R) calibration determines the entire wavelength grid, whereas the RAD calibration estimates only wavelength shifts relative to a predefined grid. During initialization, IRR(R) processing constructs the initial wavelength grid using Chebyshev polynomials. Meanwhile, RAD processing uses wavelengths extracted from the latest-measured solar irradiance spectra as the initial input, against which the shifts are estimated.

To obtain reference spectra, the IRR(R) processing convolves a high-resolution reference solar spectrum (version 2 of the Total and Spectral Solar Irradiance Senser-1 Hybrid Solar Reference Spectrum; Coddington et al., 2021, 2023), using super-Gaussian slit function parameters (Beirle et al., 2017). On the other hand, the RAD processing employs pre-convolved spectra, the spectrally calibrated TEMPO solar irradiances from the first-light measurement on August 1, 2023. By using TEMPO irradiance measurements as the reference spectra in RAD spectral calibration, we aim to reduce fitting residuals by canceling out a significant portion of the systematic radiometric error.

In spectral fitting, the state vectors for both IRR(R) and RAD involve coefficients of the Chebyshev polynomials; however, they are employed for different purposes. The IRR(R) processing uses them to construct the entire wavelength grid. In Version 3, 1st- and 2nd-degree

polynomials are used for the UV and VIS CCDs, respectively, to construct the grid for each spatial CCD position. Meanwhile, the RAD processing uses them to account for wavelength-dependent spectral shifts, i.e., the differences between the resultant and reference wavelength grids. The Version 3 RAD processing uses a 0th-degree polynomial at each spatial position, fitting a single, spectrally independent shift for each CCD. The RAD spectral calibration derives the wavelength shifts using fitting windows of 320–340 nm and 630–650 nm for the UV and VIS CCDs, respectively. These windows were selected to avoid significant signal saturation. The derived shift values are applied uniformly to all spectral pixels within each CCD.

One major difference in the state vector composition between IRR(R) and RAD is that the latter incorporates parameters that account for atmospheric processes, including the Ring effect and absorption by key trace gases: O_3 and collision-induced oxygen absorption (O_2–O_2) for UV, and O_2, O_2–O_2, and water vapor for VIS. The optical depths of these parameters are fitted along with the spectral shift. Another significant difference is that the IRR(R) state vector includes the super-Gaussian slit function parameters by default. In IRR(R), the high-resolution reference solar spectrum is iteratively convolved with the slit function to improve fitting performance.

The IRR and IRRR processing ends with spectral calibration, with the corresponding Level 1b files generated (see Figure 3). With a narrow fitting window, the IRR(R) spectral calibration can be used to derive in-flight slit function shapes for specific channels. Since the operational Version 3 Level 0-1 processor performs spectral fitting across the full spectral range of each CCD, this narrow-window capability is not implemented operationally. However, by applying this option offline, we can monitor potential temporal changes in the slit function shape for specific channels, as demonstrated in Hou et al. (2025).

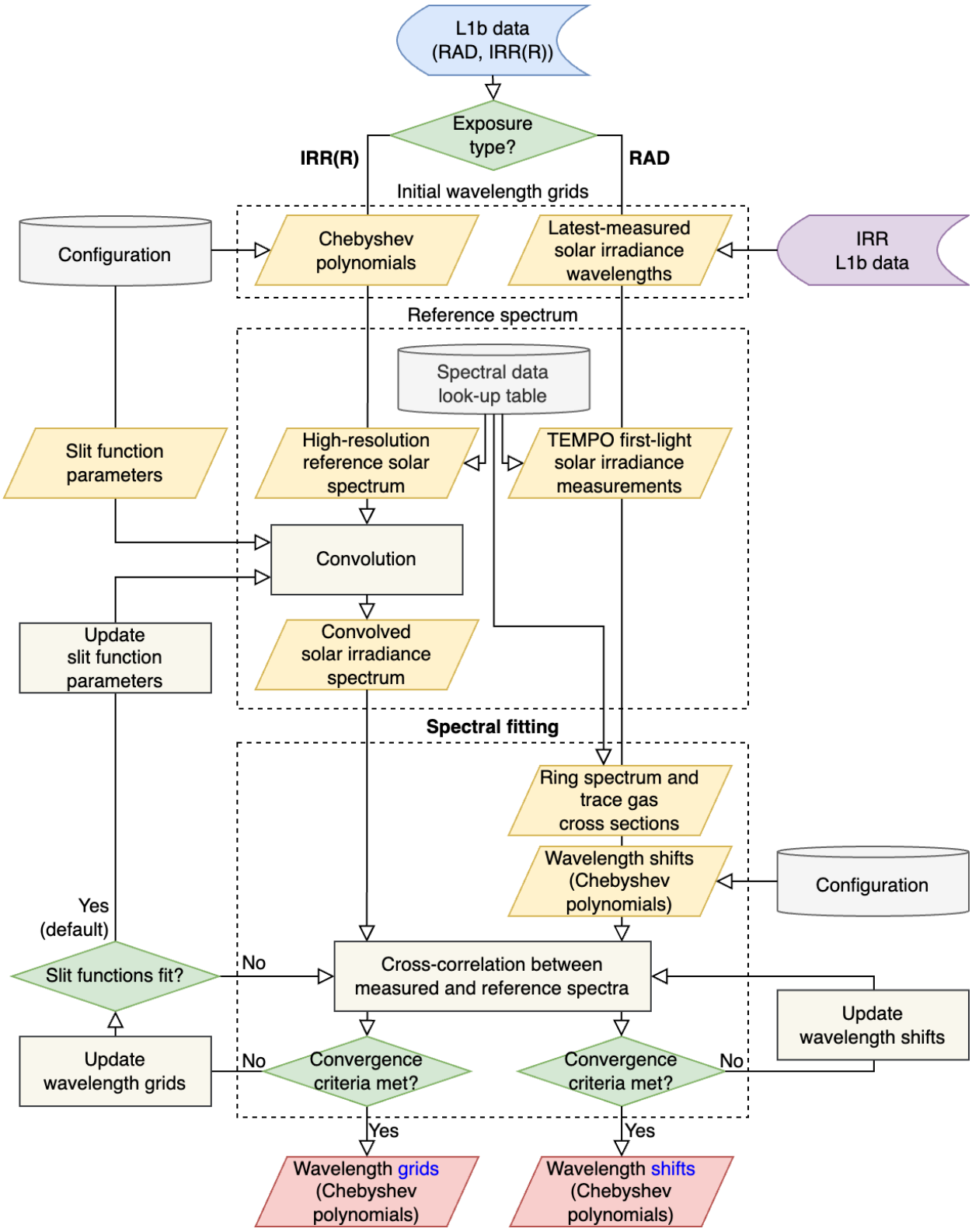

Figure 9. Flow chart of the TEMPO spectral calibration algorithm. The same algorithm is applied separately to each CCD (UV and VIS).

4 Algorithm Verification Using In-Flight Measurements

We have verified the Level 0-1 processor using in-flight measurements since the TEMPO launch, some of which have prompted version updates. Sections 4.1–4.3 describe the verifications of image processing, INR, and spectral calibration, respectively. In Section 4.4, we briefly discuss the verification of Sun-normalized radiance, an essential quantity for deriving trace gas amounts.

4.1 Image Processing

4.1.1 Octant Phase Identification

The octant phase identification requires pre-assigned gain values correctly paired with odd and even trailing columns (Section 3.1.2). To implement this, we conducted an experiment using the first-light solar irradiance data from August 1, 2023. The idea for the experiment is to switch the gain values between the two octants in each quadrant. The premise is that the incorrect offset-gain pairing should induce artificial spatial oscillations in solar irradiance data, intensifying the contrasts between high and low values. Figure 10 shows the experiment results, with solar irradiance values calculated using Equation 13. Indeed, the right panels of Figure 10 exhibit artificial oscillations in the spatial dimension, implying the pairing is incorrect. After identifying the correct offset-gain pairing, shown in the left panels, we assigned the appropriate gain for each octant before processing the Level 1 data. As shown in the left panels of Figure 10, the mean offset values of even columns were higher than those of odd columns in all quadrants of the first-light solar irradiance image. If the relative magnitudes are inverted in a quadrant for a given image frame, the processor automatically swaps the gain values between even and odd columns (see Section 3.1.2).

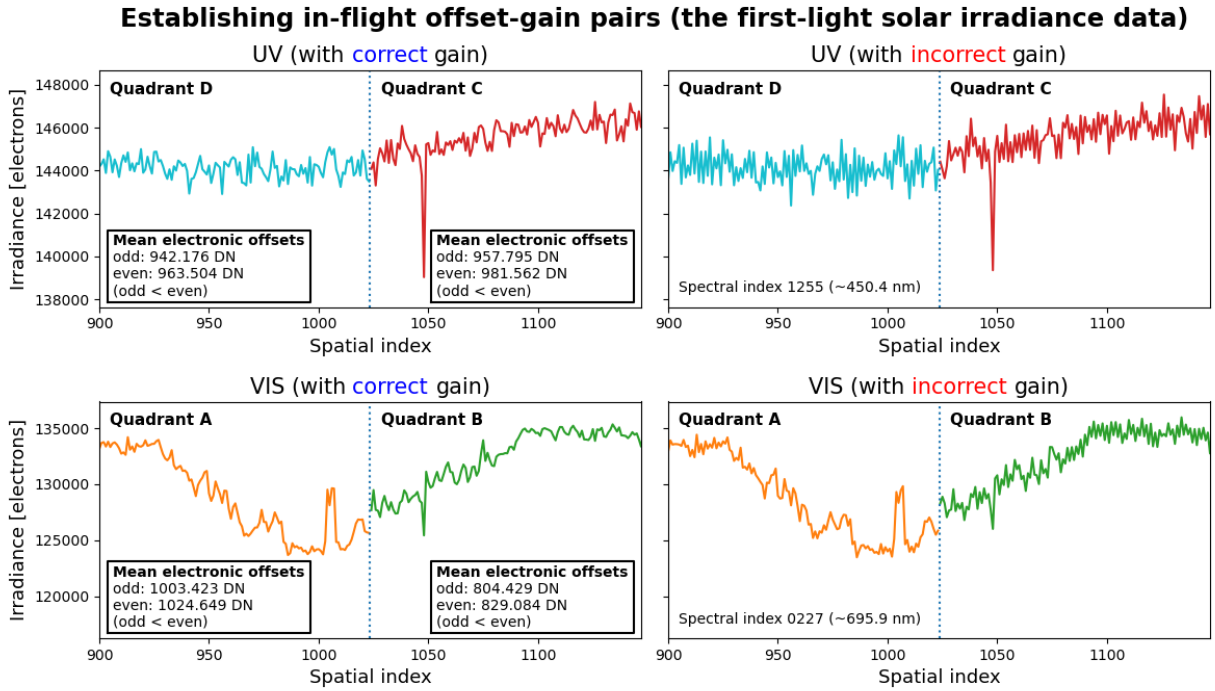

Figure 10. Establishment of in-flight offset-gain pairs using the first-light solar irradiance data from August 1, 2023. Spectral indices representing the UV and VIS CCDs are indicated inset on the right panels. The mean electronic offsets for the correct offset-gain pairs are presented on the left panels.

902 4.1.2 Electronic Offset Correction

903 To verify which is more suitable between the two electronic offset correction methods
904 (row-independent and row-by-row), we analyzed in-flight measurement data from August 18,
905 2023, when image-region dark current was measured with different integration-time
906 configurations. The measurement set included dark signals measured with $t_{\mathrm{int}} = 0$. In this case,
907 D_{dc} in Equation 7 corresponds to zero, resulting in
908
909 $$C_{\mathrm{meas,dc}}(p,s)(t_{\mathrm{int}} = 0) = [D_{\mathrm{smr}} + D_{\mathrm{sdc,read}} + D_{\mathrm{ext}} + D_{\mathrm{eoff}}](p,s) \times N_{\mathrm{co}}. \quad (35)$$
910
911 According to Equations 7 and 35, the pure image-region dark signal D_{dc} can be theoretically
912 derived by subtracting $C_{\mathrm{meas,dc}}(p,s)(t_{\mathrm{int}} = 0)$ from $C_{\mathrm{meas,dc}}(p,s)$.
913 Figure 11a shows the mean pure image-region dark currents ($D_{\mathrm{dc}}/t_{\mathrm{int}}$, in units of DN s^{-1})
914 as a function of integration time, derived with the two different offset corrections for each octant.
915 This panel indicates that employing row-independent (constant) offsets results in less stable dark
916 currents, especially with short integration times. Therefore, we decided to employ the row-by-
917 row configuration. Figure 11b shows changes in the mean electronic offset for each octant.
918 Assuming the offset values are independent of integration time, these changes can be interpreted
919 as time-dependent variations within ~30 minutes of consecutive measurements. The Level 0-1
920 processor performs the electronic offset correction on a frame-by-frame basis, accounting for this
921 time-dependent offset variation.
922
923 4.1.3 Smear Correction
924 Figure 11c compares the smear signals estimated using the two approaches (the overclock
925 method and time-based scaling) based on dark current measurements taken on August 18, 2023,
926 with multiple integration times. Only co-adding and electronic offset corrections were applied to
927 the Level 0 data (Equations 9 and 10), resulting in smear signals in units of DN. With zero
928 integration time, the signals remaining in the photoactive regions after the two corrections
929 correspond to $D_{\mathrm{smr}} + D_{\mathrm{sdc,read}} + D_{\mathrm{ext}}$ (see Equation 35). Considering the small contribution of
930 D_{ext} with typical crosstalk coefficients of ~0.0015, the higher smear signals estimated by the
931 overclock method can be attributed to higher $D_{\mathrm{sdc,read}}$ at the smear rows, which stay in the
932 storage regions for longer than the photoactive rows during read-out. Regardless of the length of

integration time, the overclock-estimated smear signals persist in higher values than the average signal range from the photoactive regions at zero integration time, possibly due to the consistent contribution of $D_{\mathrm{sdc,read}}$. Meanwhile, the smear signals estimated using the time-based scaling approach decrease as integration time increases. Ideally, in this analysis, the time-based scaling should estimate smear signals for each CCD column as $(\overline{D_{\mathrm{dc}}}+D_{\mathrm{smr}}) \times [t_{\mathrm{ft}}/(t_{\mathrm{int}} + t_{\mathrm{ft}})]$, where $\overline{D_{\mathrm{dc}}}$ represents the photoactive-column-averaged D_{dc}. However, in practice, $D_{\mathrm{sdc,read}}$ cannot be removed before or during smear correction. As a result, the calculation follows: $\left(\overline{D_{\mathrm{dc}}} + D_{\mathrm{smr}} + \overline{D_{\mathrm{sdc,read}}}\right) \times [t_{\mathrm{ft}}/(t_{\mathrm{int}} + t_{\mathrm{ft}})]$, where $\overline{D_{\mathrm{sdc,read}}}$ represents the photoactive-column-averaged $D_{\mathrm{sdc,read}}$ (the contribution of D_{ext} is neglected). Since $D_{\mathrm{sdc,read}}$ is independent of t_{int}, increasing t_{int} reduces the relative contribution of $D_{\mathrm{sdc,read}}$ in the estimated smear signal, leading to the decreasing trend shown in Figure 11c.

For integration times of Sun (72 or 68.3 ms) and Earth (100 ms) exposure or longer, the two smear estimation methods exhibit significantly different results (Figure 11c). From the perspective of contamination by $D_{\mathrm{sdc,read}}$, the time-based scaling method offers an advantage, leading to enhanced accuracy at low signal levels. The Version 3 Level 0-1 processor therefore employs the time-based scaling method for all exposure types. However, in this method, excluding bad pixels from the column average calculation can impact smear estimation, especially when saturation occurs over clouds during Earth scans. The current approach represents a consistent and effective implementation for Version 3. Future versions will explore an optimization for each exposure type to further improve performance.

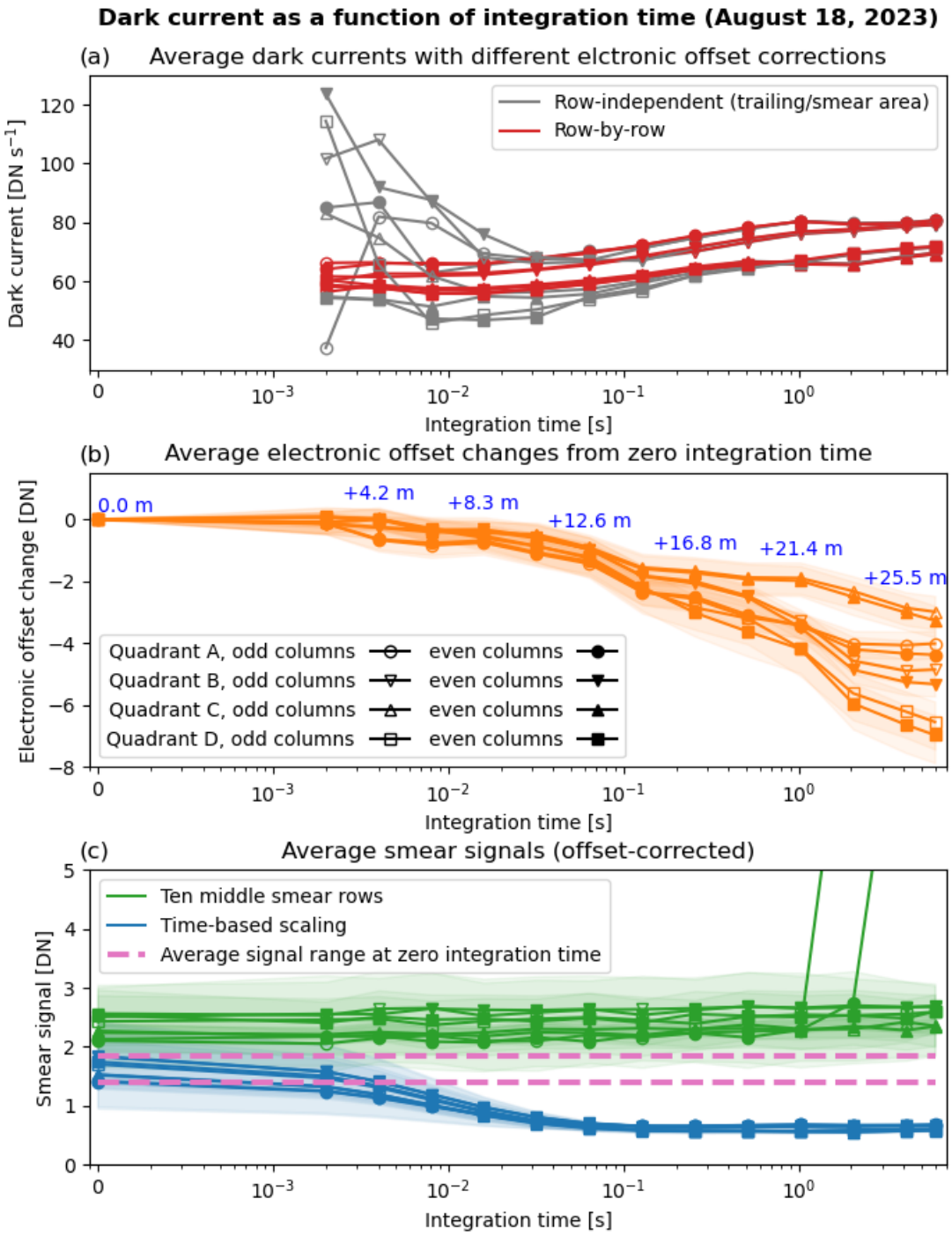

Figure 11. Dark current, electronic offset, and smear as functions of integration time. For the analyses, dark current measurements from August 18, 2023, were used. During the measurements, integration time gradually increased from 0 to 6 seconds. The blue text in panel (b) indicates the elapsed time in minutes from the first measurement with zero integration time.

959 4.1.4 Bidirectional Transmittance Distribution Function (BTDF) Correction
960 The on-ground calibration characterized the diffuser transmittances as a function of the
961 incident elevation angle, providing the following equation for elevation-angle-based BTDF
962 correction:
963
964 $$\tau(\lambda, s) = \tau_{\mathrm{LUT}}(\lambda, s) \times (1 + e). \quad (36)$$
965
966 This BTDF correction approach was used in the Version 1 Level 0-1 processor.
967 During the commissioning phase, however, we noticed distinct temporal change patterns
968 in solar irradiance across spatial CCD positions, even after correcting for incident elevation angle.
969 Figure 12a shows variations in solar irradiance data at three different spatial positions over a
970 one-year period following first light (August 1, 2023–August 1, 2024), after elevation-angle
971 correction. To enhance the performance of the BTDF correction, we incorporated the scattering
972 angle in addition to the elevation angle (see Figure 7) and added an extra elevation angle
973 correction. As a result, Equation 36 was replaced with Equation 30 in the Versions 2 and 3 Level
974 0-1 processor, as described in Section 3.1.2.
975 Figure 12b presents the temporal variations in solar irradiance for the same three spatial
976 CCD positions as in Figure 12a after applying the updated BTDF correction. The dispersed
977 pattern seen in Figure 12a is significantly mitigated. The cause of the remaining trends is to be
978 investigated, including the possibility that the goniometry dependence is undercorrected. It is
979 noteworthy that spatial position 1023 shows temporal changes, even though it is located in the
980 central part of the CCD, where the diffuser transmittance is least sensitive to variations in the
981 diffuser azimuth angle. The remaining increase or decrease patterns may be attributed to
982 temporal changes in the spectral shift, as a fixed spectral index does not always represent the
983 same wavelength. Diffuser degradation has not been considered either.
984
985

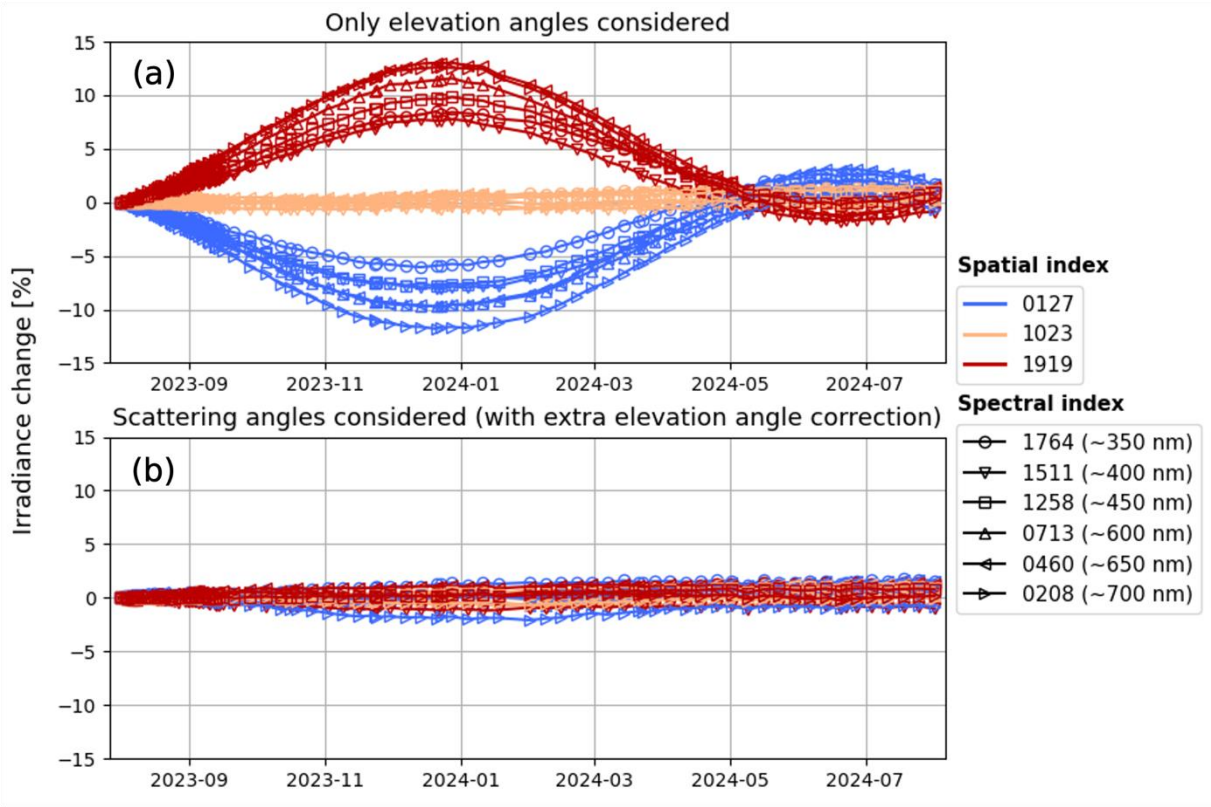

Figure 12. Update of BTDF correction. (a) temporal changes in solar irradiance depending on spatial and spectral CCD indices when only elevation angles are considered for BTDF correction; (b) same as panel (a), but when scattering angles are considered with extra elevation angle correction.

4.1.5 Error Estimation

On August 17, 2023, TEMPO measured fifteen consecutive solar irradiance frames instead of one nominal frame as part of the commissioning, offering an opportunity to quantify the random variability in irradiance measurements. Using the 15 frames, we derived the variance for each CCD pixel to evaluate the reliability of the irradiance error estimates ($\varepsilon_{\mathrm{meas}}$) from the Level 0-1 processor. In addition to the random variability, however, the irradiance magnitudes vary during multiple frame measurements due to the diffuser angle changes. To account for the angle changes, we first scaled each irradiance frame so that the spectrum at each spatial CCD position has the same mean magnitude as the 15-frame average for that position. We then calculated the standard deviation using 15 samples for each spatial and spectral position, which can be interpreted as a random error. The blue curve in Figure 13 shows the SNRs calculated with these variance-based random errors for the spatial CCD position of 1023. Considering the number of frames (15) was not sufficient to derive stable standard deviations, we applied spectral smoothing using a median filter with a 25-spectral-pixel window (the orange curve in Figure 13). The SNRs calculated using $\varepsilon_{\mathrm{meas}}$ (i.e., the model-estimated SNRs) are presented with the green curve in Figure 13. The smoothed, variance-based SNRs and the model-estimated SNRs exhibit a strong agreement, demonstrating a robust reliability of the irradiance errors estimated using the TEMPO Level 0-1 processor.

We verified whether the in-flight irradiance SNRs calculated for August 17, 2023, met the requirements. The SNR requirements were determined at 16 wavelengths (Table 4). The green circles in Figure 13 indicate the model-estimated SNRs sampled at those wavelengths, except for 290 nm, for which we sampled the SNR at 292.1 nm owing to the practical TEMPO spectral coverage. The red circles represent the TEMPO SNR requirements. The comparison between the green and red circles in Figure 13 demonstrates that the in-flight irradiance SNR meets the requirement at every wavelength. To extend the SNR verification beyond spatial index 1023, we calculated the median SNR for each wavelength across all fully illuminated spatial CCD positions (5–2040). Table 4 summarizes the verification result, indicating that the achieved median SNR is higher than the requirement at every wavelength.

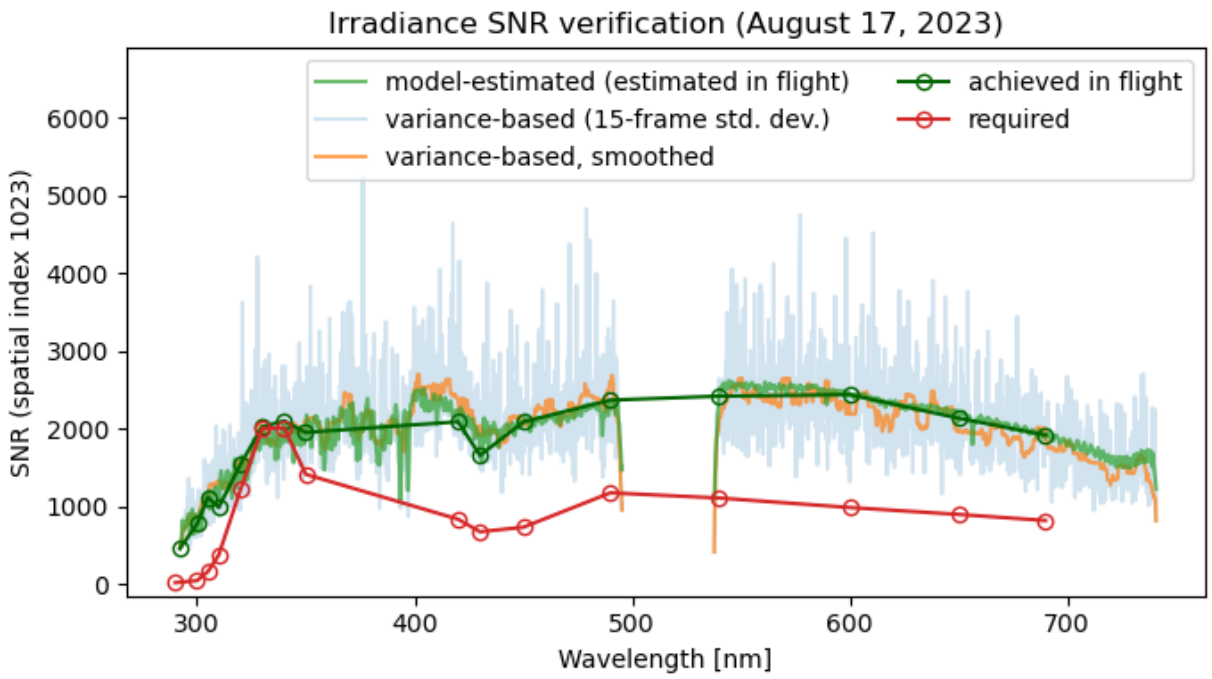

Figure 13. SNR verification for solar irradiances measured on August 17, 2023. The spatial CCD position of 1023 (0-based) was chosen. The green curve represents SNRs calculated using the irradiance errors estimated in flight. The green circles indicate the SNR values at the wavelengths where the pre-launch SNR requirements were specified. The required SNRs are presented with red circles. The blue curve represents SNRs calculated using standard deviations of fifteen consecutive irradiance frames in place of the estimated irradiance errors. The orange curve shows the result of smoothing the blue curve using a median filter with a 25-spectral-pixel window.

The SNR requirements for Earth radiance are identical to those for solar irradiance, but under the condition of 4-pixel binning and a nominal radiance assigned for each of the 16 wavelengths. To verify the in-flight radiance SNRs, we used measurements from September 1, 2023, when we tested TEMPO's maximum spatial coverage during commissioning. First, we collected TEMPO pixels having radiances within a ±5% range of the nominal radiance for each wavelength, using all 13 granules of the 10th scan on that day. The lower panel of Figure 14 shows the nominal radiances and the medians of the sampled radiances. We then calculated the median of radiance errors ($\varepsilon_{\mathrm{meas}}$) for the collected TEMPO pixels at each wavelength. Finally, assuming the SNR is proportional to the square root of the number of binned pixels, we doubled the ratio of the median radiance to the median error for each wavelength to represent the 4-pixel binned condition. The upper panel of Figure 14 presents the required and in-flight radiance SNRs. The SNR values are also summarized in Table 4, which shows that the in-flight values meet the requirements for 320–690 nm, while the estimates are slightly smaller than the requirements for 290–310 nm. Since this verification used only 13 granules, a more robust analysis could be achieved by incorporating a larger dataset in future studies. Furthermore, the in-flight SNR estimates for 290–310 nm may change with stray light correction updates in future Level 0-1 processor versions.

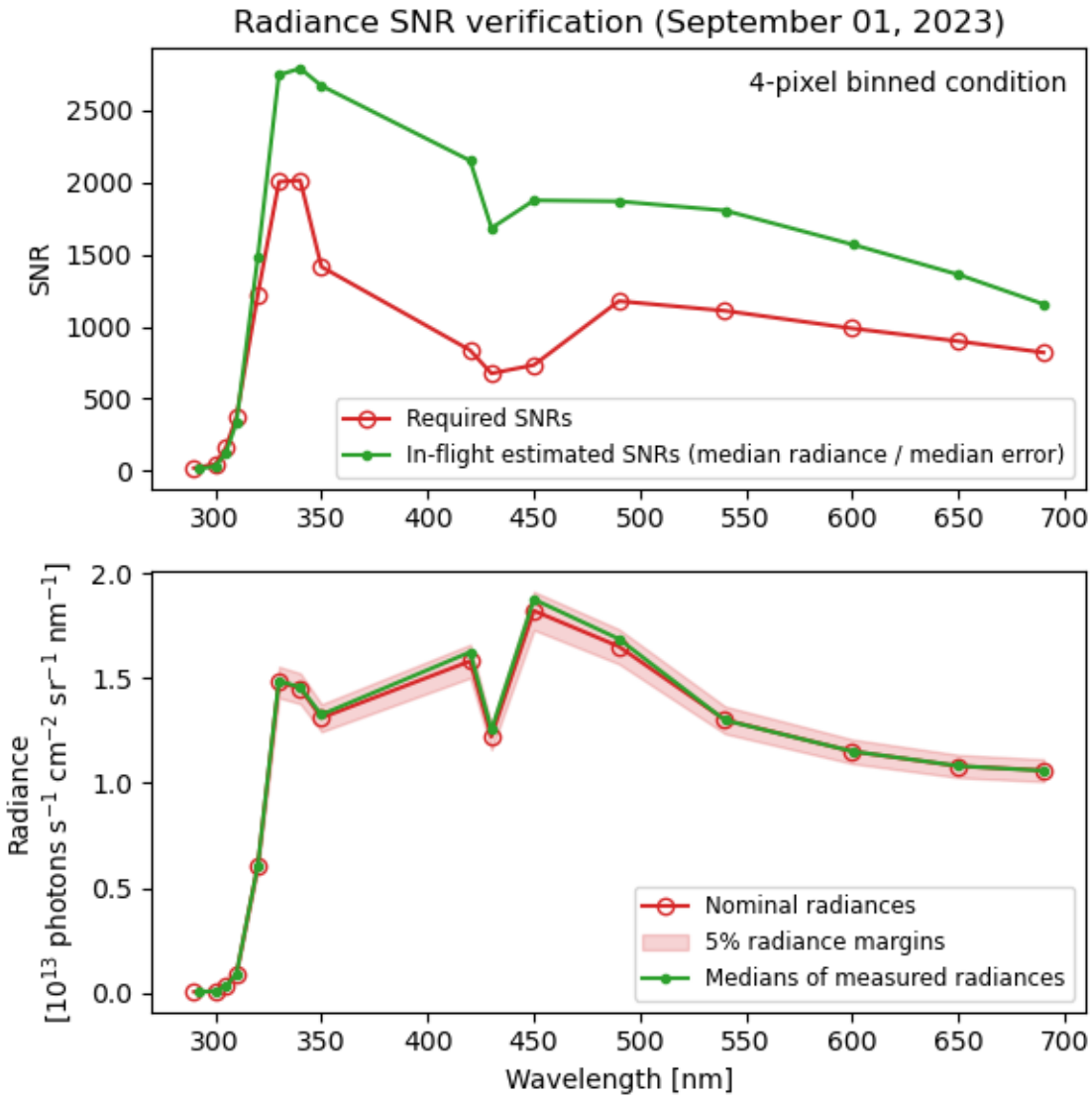

Figure 14. SNR verification for Earth radiances measured on September 1, 2023. The lower panel shows, for each wavelength, the nominal radiance for the required SNR, along with the median of sampled radiance measurements within a ±5% range of the nominal radiance. The upper panel shows the required SNR and the median of sampled SNRs for each wavelength.

Table 4. Required and achieved SNRs. The in-flight solar irradiance SNRs were derived using measurements from August 17, 2023. The in-flight radiance SNRs were calculated using data from September 1, 2023. The irradiance and radiance SNR requirements have identical values, but the 4-pixel binned condition is applied to the radiance requirements.

Wavelength (nm)	Required SNR	In-flight achieved solar irradiance SNR	In-flight achieved Earth radiance SNR (4-pixel binned)
290	19.6	445.5 (292.1 nm)	15.2 (292.1 nm)
300	46.1	772.1	30.2
305	161.9	1101.2	124.8
310	377.0	982.3	334.3
320	1220.0	1532.4	1484.6
330	2003.0	2008.0	2743.1
340	2013.0	2080.5	2788.4
350	1414.0	1951.5	2668.5
420	836.0	2077.5	2149.6
430	675.0	1652.6	1682.2
450	733.0	2074.6	1874.2
490	1176.0	2354.8	1867.5
540	1109.0	2482.8	1803.6
600	987.0	2423.9	1568.7
650	898.0	2120.6	1359.1
690	820.0	1883.3	1155.0

4.2 Image Navigation and Registration (INR)

INR requirements apply during daylight only. Figure 15 and Table 5 show the representative INR performance as determined from independently matched tie-points against GOES-R reference imagery. TEMPO is required to navigate its pixels to within 82 μrad of its actual location in TEMPO scan coordinates. Generally, performance is subpixel and well within the specifications.

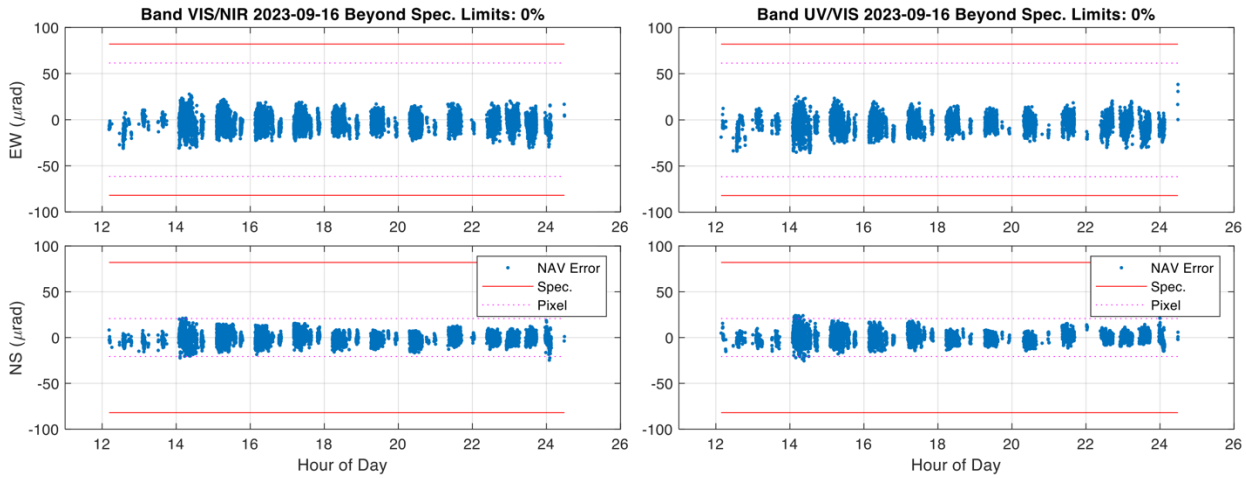

Figure 15. Representative INR system performance as determined from independently matched tie-points against GOES-R reference imagery (September 16, 2023). The upper and lower rows represent East-West and North-South dimensions, respectively. The left and right columns show results for the VIS and UV channels, respectively. The blue dots represent navigation errors (NAV Error), the red solid lines indicate the specification requirements (Spec.), and the red dotted lines show pixel sizes (Pixel).

Table 5. Statistics for representative system performance as determined from independently matched tie-points against GOES-R reference imagery (September 16, 2023).

Channel	Number of data points	East-West mean (μrad)	East-West std. dev. (μrad)	North-South mean (μrad)	North-South std. dev. (μrad)	Out of limit
VIS	34136	–2.0981	6.0594	–1.4832	4.1732	0
UV	28569	–3.3226	6.1935	–0.1280	4.3225	0

4.3 Spectral Calibration

Figure 16 presents wavelength differences detected in the first-light solar irradiance measurements relative to the pre-launch wavelength grids. We derived Chebyshev-polynomial-based wavelength grids for the first-light image, following the procedures described in Section 3.3, and compared them with the on-ground instrument calibration results. Significant differences were found in both the UV and VIS CCDs, highlighting the necessity of in-flight calibration. As described in Section 3.3, the Level 0-1 processor derives the wavelength grid for every solar irradiance image, and the result is used for Level 2 retrievals and instrument stability monitoring.

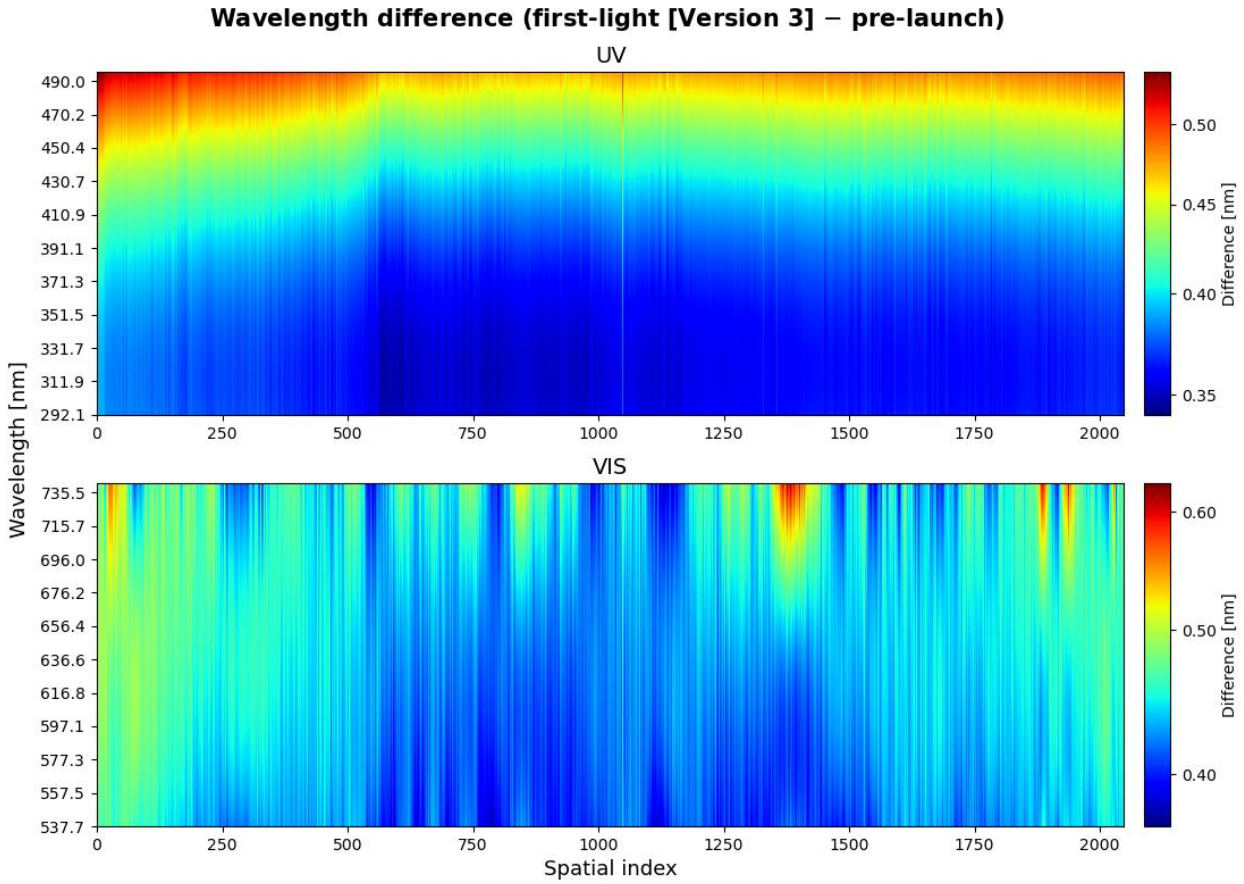

Figure 16. Wavelength shifts detected in the first-light solar irradiance measurements in comparison to the pre-launch wavelength grids.

4.4 Sun-normalized radiance

Figure 17 displays the Earth radiance image taken from the very first TEMPO scan. The scan started at 15:12:49 UTC on August 2, 2023. The TEMPO instrument successfully captured aerosol plumes from a wildfire transported from Canada to the Eastern US and to the Atlantic. Figure 17 also presents spectral structures of radiance and Sun-normalized radiance samples selected for four different surface types, measured on the same day. Not only were the surface features successfully captured, including the vegetation red edge (>680 nm), but atmospheric features were also clearly detected, such as O_3 Huggins-band absorption (300–350 nm), Ring effect (390–400 nm), oxygen B-band (685–695 nm) and γ-band (~628 nm) absorption, and water vapor absorption (580–740 nm) (Burrows et al., 1999; Chance, 2006; González Abad et al., 2019). These examples demonstrate the high performance of the TEMPO instrument and the Level 0-1 processor.

However, recent assessments indicate that Sun-normalized radiances from TEMPO are generally overestimated compared to radiative transfer simulations and other satellite measurements. The biases have been estimated to be on the order of 10%, with possible signal and wavelength dependence. To address this, we have assessed solar irradiance and Earth radiance, with the latter using ABI measurements from the GOES-16 and GOES-19 satellites. As a detailed radiometric assessment is beyond the scope of this work, we validate TEMPO spectra in a separate paper. Enhancing absolute calibration is among the highest priorities for future updates to the TEMPO Level 0-1 processor.

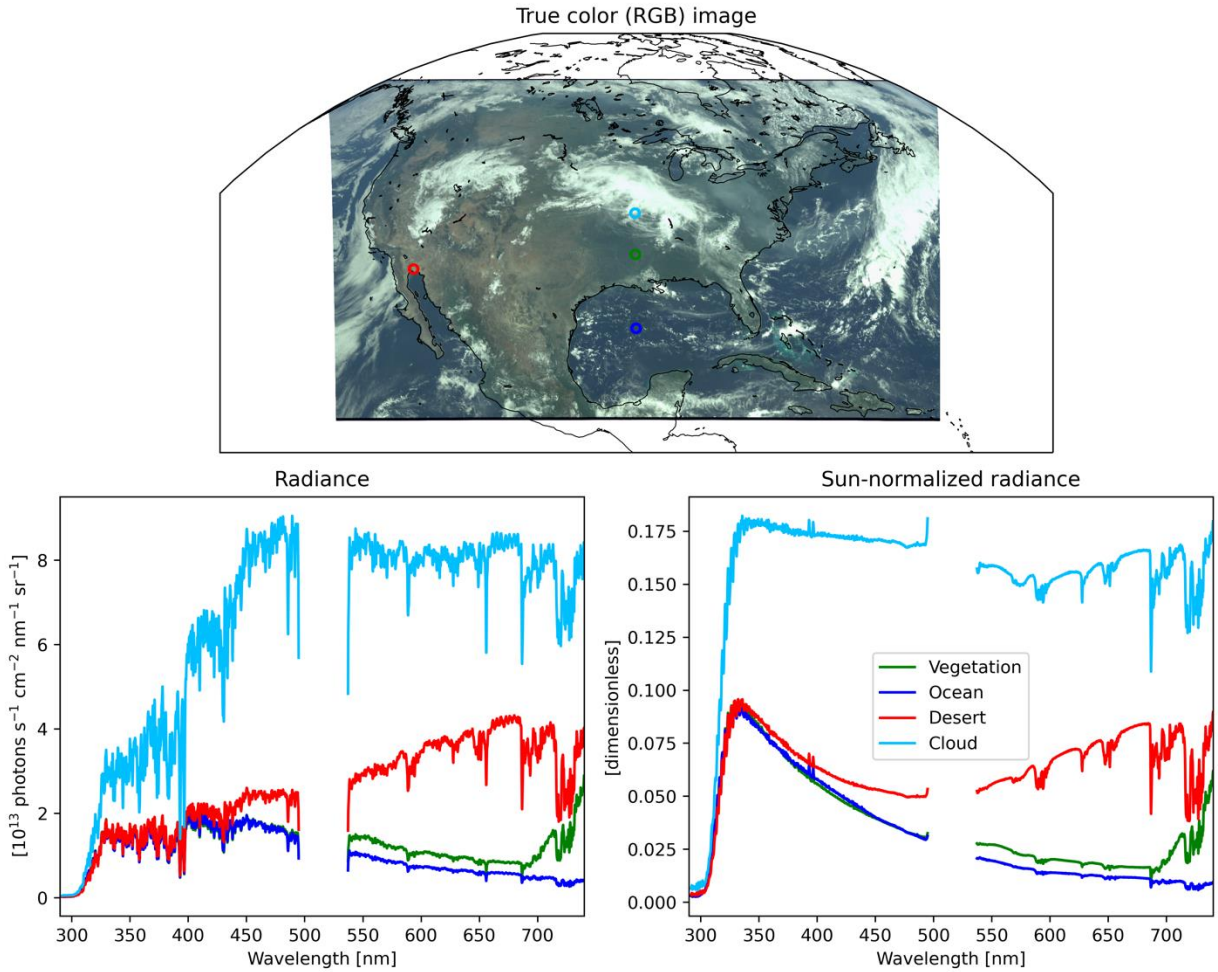

Figure 17. The Earth image taken from the first TEMPO scan. Samples of radiance and Sun-normalized radiance spectra are presented for four different surface types: vegetation, ocean, desert, and partial cloud.

5 Summary

The TEMPO Level 0-1 processor converts digitized signals downlinked from the satellite (Level 0) into physical quantities, producing dark current (Level 1a), solar irradiance (Level 1b), and geolocated Earth radiance (Level 1b) as its main outputs. The Level 1b products serve as essential inputs for Level 2 retrievals, which monitor air quality over North America using trace gases, such as O_3, NO_2, and HCHO.

Since its initial development, the TEMPO Level 0-1 processor has undergone significant updates to enhance the radiometric and spectral quality of the Level 1 products, along with improvements in geolocation accuracy. The Version 3 products incorporate instrument characteristics derived on orbit as well as on-ground calibration results.

The Version 3 Level 0-1 processor consists of three main algorithm components: image processing, INR, and spectral calibration. Although polarization correction is integrated into the processor, it has been deactivated. Appendix B of this article outlines the theoretical basis of polarization correction; its practical impact on in-flight measurements is being investigated separately.

Since Version 3 Sun-normalized radiances are found to be overestimated, future updates will adjust the absolute calibration by revisiting the pre-launch calibration key data. Other Level 0-1 processor components, including stray light correction, will also be improved. Instrument degradation will continue to be monitored to assess its impact over time and will be corrected in future updates.

Appendix A: Algorithm Input and Output Variables

The Level 0 files for the five different exposure types have the same file structure (DRK, RAD, RADT, IRR, and IRRR). Table A1 lists key Level-0 variables used for the Level 0-1 processing. Tables A2–A4 present key output variables in the Level-1 DRK, RAD(T), and IRR(R) products, respectively.

Table A1. Key variables in the Level 0 product

Name	Long name	Unit
ccd_int_type	CCD integration type used when FPE is commanded to imaging	-
exposure_time	Exposure time	seconds
frame_transfer_time	Frame transfer time	seconds
readout_time	Read-out time	seconds
num_coadds	Number of co-adds	-
num_dg_rows	Starting row of storage-region aggregation	-
num_tg_rows	Number of storage-region rows aggregated	-
image	Digital counts	digital number (DN)
image_start_time	Exposure start time for each frame	seconds since 1980-01-06T00:00:00Z

1140 **Table A2.** Key variables in the DRK product.

Name	Long name	Unit
/frames/ image	Dark current for each frame	electrons s^{-1}
/frames/ mean_dark_current	Mean dark current in each quadrant for each frame	electrons s^{-1}
/frames/ mean_sdc	Mean storage region dark current in each quadrant for each frame	electrons s^{-1}
/frames/ pixel_quality_flag	Pixel quality flag for each frame	-
/frames/ image_start_time	Exposure start time for each frame	seconds since 1980-01-06T00:00:00Z
image	Average of '/frames/image' over multiple frames	electrons s^{-1}
mean_dark_current	Average of '/frames/mean_dark_current' over multiple frames (per quadrant)	electrons s^{-1}
mean_sdc	Average of '/frames/mean_sdc' over multiple frames (per quadrant)	electrons s^{-1}
pixel_quality_flag	Pixel quality flag for the 'image' variable	-
image_start_time	Average of '/frames/image_start_time' over multiple frames	seconds since 1980-01-06T00:00:00Z

1141

1142 **Table A3.** Key variables in the RAD and RADT products.

Name	Long name	Unit
/band_290_490_nm/ radiance	Earth radiance (UV CCD)	photons s^{-1} cm^{-2} nm^{-1} sr^{-1}
/band_290_490_nm/ radiance_error	Earth radiance error (UV CCD)	photons s^{-1} cm^{-2} nm^{-1} sr^{-1}
/band_290_490_nm/ pixel_quality_flag	Pixel quality flag (UV CCD)	-
/band_290_490_nm/ ground_pixel_quality_flag	Ground pixel quality flag (UV CCD)	-
/band_290_490_nm/ nominal_wavelength	Wavelength (UV CCD)	nm
/band_290_490_nm/ latitude	Latitude at pixel center (UV CCD)	degree North (°N)
/band_290_490_nm/ latitude_bounds	Latitude bounds (NE, NW, SW, SE) (UV CCD)	degree North (°N)
/band_290_490_nm/ longitude	Longitude at pixel center (UV CCD)	degree East (°E)
/band_290_490_nm/ longitude_bounds	Longitude bounds (NE, NW, SW, SE) (UV CCD)	degree East (°E)
/band_290_490_nm/ solar_azimuth_angle	Solar azimuth angle (UV CCD)	degree (°)
/band_290_490_nm/ solar_zenith_angle	Solar zenith angle (UV CCD)	degree (°)
/band_290_490_nm/ viewing_azimuth_angle	Viewing azimuth angle (UV CCD)	degree (°)
/band_290_490_nm/ viewing_zenith_angle	Viewing zenith angle (UV CCD)	degree (°)
/band_290_490_nm/	Fraction of pixel area covered	-

snow_ice_fraction	by snow and/or ice (UV CCD)	
/band_540_740_nm/ terrain_height	Area-weighted mean terrain height inside each pixel (UV CCD)	m
/band_540_740_nm/ radiance	Earth radiance (VIS CCD)	photons s^{-1} cm^{-2} nm^{-1} sr^{-1}
/band_540_740_nm/ radiance_error	Earth radiance error (VIS CCD)	photons s^{-1} cm^{-2} nm^{-1} sr^{-1}
/band_540_740_nm/ pixel_quality_flag	Pixel quality flag (VIS CCD)	-
/band_540_740_nm/ ground_pixel_quality_flag	Ground pixel quality flag (VIS CCD)	-
/band_540_740_nm/ nominal_wavelength	Wavelength (VIS CCD)	nm
/band_540_740_nm/ latitude	Latitude at pixel center (VIS CCD)	degree North (°N)
/band_540_740_nm/ latitude_bounds	Latitude bounds (NE, NW, SW, SE) (VIS CCD)	degree North (°N)
/band_540_740_nm/ longitude	Longitude at pixel center (VIS CCD)	degree East (°E)
/band_540_740_nm/ longitude_bounds	Longitude bounds (NE, NW, SW, SE) (VIS CCD)	degree East (°E)
/band_540_740_nm/ solar_azimuth_angle	Solar azimuth angle (VIS CCD)	degree (°)
/band_540_740_nm/ solar_zenith_angle	Solar zenith angle (VIS CCD)	degree (°)
/band_540_740_nm/ viewing_azimuth_angle	Viewing azimuth angle (VIS CCD)	degree (°)

/band_540_740_nm/ viewing_zenith_angle	Viewing zenith angle (VIS CCD)	degree (°)
/band_540_740_nm/ snow_ice_fraction	Fraction of pixel area covered by snow and/or ice (VIS CCD)	-
/band_540_740_nm/ terrain_height	Area-weighted mean terrain height inside each pixel (VIS CCD)	m

1143

1144 **Table A4.** Key variables in the IRR and IRRR products.

Name	Long name	Unit
/band_290_490_nm/ irradiance	Solar irradiance (UV CCD)	photons s^{-1} cm^{-2} nm^{-1}
/band_290_490_nm/ irradiance_error	Solar irradiance error (UV CCD)	photons s^{-1} cm^{-2} nm^{-1}
/band_290_490_nm/ pixel_quality_flag	Pixel quality flag (UV CCD)	-
/band_290_490_nm/ nominal_wavelength	Wavelength (UV CCD)	nm
/band_290_490_nm/ wavecal_params	Wavelength calibration parameters	-
/band_540_740_nm/ irradiance	Solar irradiance (VIS CCD)	photons s^{-1} cm^{-2} nm^{-1}
/band_540_740_nm/ irradiance_error	Solar irradiance error (VIS CCD)	photons s^{-1} cm^{-2} nm^{-1}
/band_540_740_nm/ pixel_quality_flag	Pixel quality flag (VIS CCD)	-
/band_540_740_nm/ nominal_wavelength	Wavelength (VIS CCD)	nm
/band_540_740_nm/ wavecal_params	Wavelength calibration parameters	-

1145

Appendix B: Polarization Correction

Even with the mitigation using a quartz wave plate (see Section 2.1), the instrument still has a sensitivity to polarized light. For Earth exposure, the source of polarization is the atmosphere. As described in Section 3.1.1, solar measurements can also be affected by polarization. In this case, the source of polarization is the diffusers. The TEMPO Level 0-1 processor includes polarization correction capability for both RAD and IRR(R) (Figure 3), with plans to activate it after thorough investigations using in-flight measurements.

The RAD and IRR(R) processing shares the identical polarization correction formula (Sun and Xiong, 2007), with different approaches to derive parameters within it:

$$I_{\text{use}} = \frac{I_{\text{meas}}^{\text{ib}}}{1+\{l\times r\times\cos[2(\chi-\phi)]\}}, \tag{B1}$$

where I_{use} represents polarization-corrected (ir)radiance (i.e., $I_{\text{meas}}^{\text{ib}} - E_{\text{pol}}$, where E_{pol} represents the perturbation caused by polarization), or useful (ir)radiance, from the Earth (Sun); l denotes the linear polarization sensitivity (LPS) of the instrument; r indicates the degree of linear polarization (DoLP); χ is the phase angle of polarization with respect to the instrument reference plane, and ϕ is the angle of maximum transmission. Figure B1 shows examples of the LPS and angle of maximum transmission of the TEMPO instrument, both as functions of wavelength.

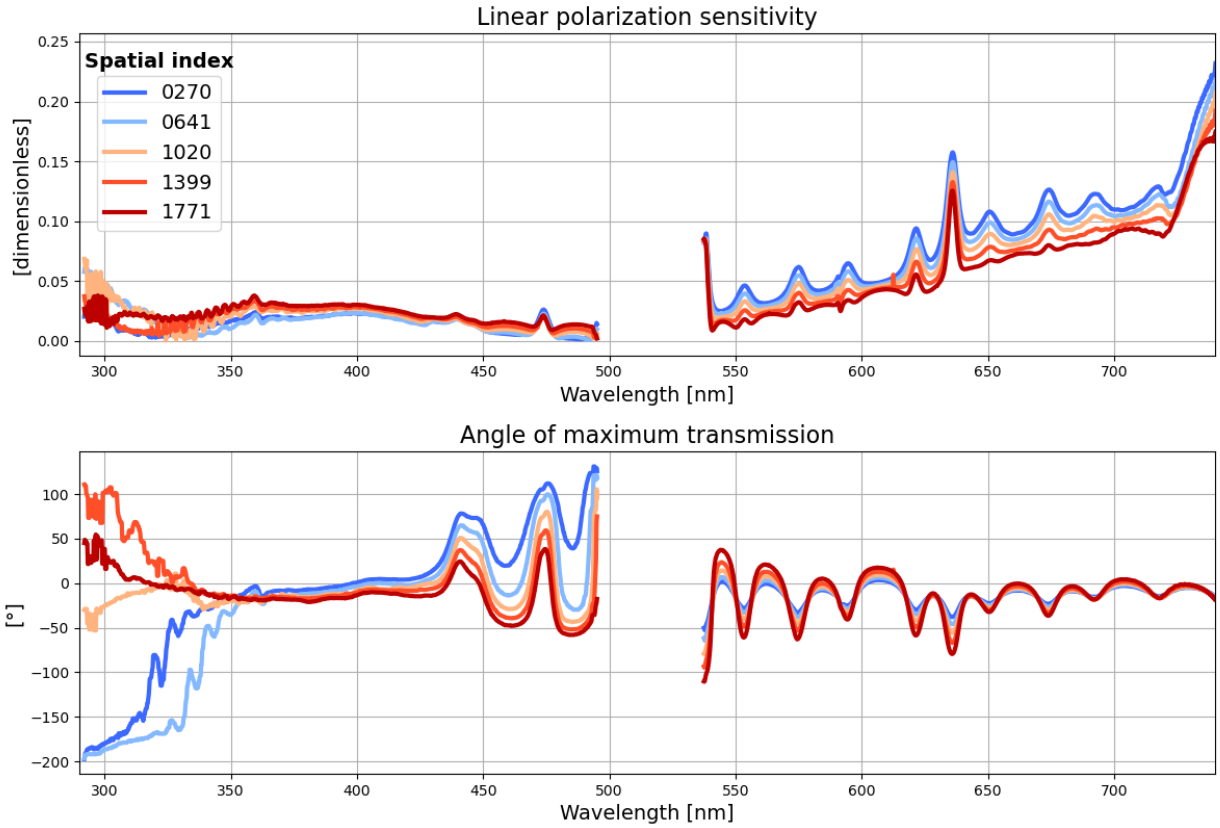

Figure B1. The linear polarization sensitivity and angle of maximum transmission of the TEMPO instrument, as a function of wavelength.

The IRR(R) and RAD polarization corrections use different approaches to calculate r and χ in Equation B1. For IRR(R), the LPS of a two-plate diffuser l_d is employed for the term r:

$$l_d = \frac{T_p^2 - T_s^2}{T_p^2 + T_s^2}, \tag{B2}$$

where T_s and T_p represent power transmission coefficients for perpendicular and parallel polarization modes, respectively. The incident azimuth angle on the diffuser (see Figure 7) is used for the term χ. In the RAD processing, the DoLP of the atmosphere and the phase angle of polarization are calculated for the terms r and χ, respectively. The RAD polarization correction has a high similarity with that for the GEMS instrument (Choi et al., 2021, 2024). Below, we describe the polarization correction algorithm for Earth exposure.

Figure B2 shows a flow chart of Earth polarization correction. The correction can be performed with the Lambertian-equivalent reflectivity (LER) or mixed LER (MLER) approaches, which treat each TEMPO spatial pixel as a single homogeneous scene or a combination of cloud and Earth surface, respectively. For the LER option, scene reflectances are initially assumed to be 0.05. The MLER option combines surface reflectances from the SCIAMACHY climatology (Tilstra et al., 2017) and cloud reflectance of 0.8 to derive initial scene reflectances. Initial total O_3 columns are derived using a climatology based on the OMI O_3 profile product or the previously derived O_3 column, if there is one.

The algorithm first derives the scene (LER) or cloud (MLER) pressure, which is followed by total O_3 column derivation. Considering the scene/cloud pressure and O_3 derivations depend on each other, these calculations are iterated twice. The derived quantities are then used to determine scene reflectance (LER) or cloud fraction (MLER). In this step, Sun-normalized radiances measured from TEMPO are compared with those obtained from a Stokes-parameter look-up table. The Stokes-parameter look-up table has seven dimensions: wavelength, scene reflectance, scene pressure, O_3 profile, solar zenith angle, viewing zenith angle, and relative azimuth angle. Here, the O_3 profile is determined using another look-up table that uses latitude and total O_3 column as parameters, which was constructed using GOME retrievals. After spectral interpolation of scene reflectance (or cloud fraction) onto every wavelength in the Stokes-parameter look-up table, the algorithm derives Stokes parameters Q and U. These Stokes parameters are employed to derive the DoLP of the atmosphere and the phase angle of polarization, which are respectively used for the terms r and χ in Equation B1. Finally, the polarization correction is conducted employing the LPS and the angle of maximum transmission for the terms l and ϕ in Equation B1, respectively (see Figure B1).

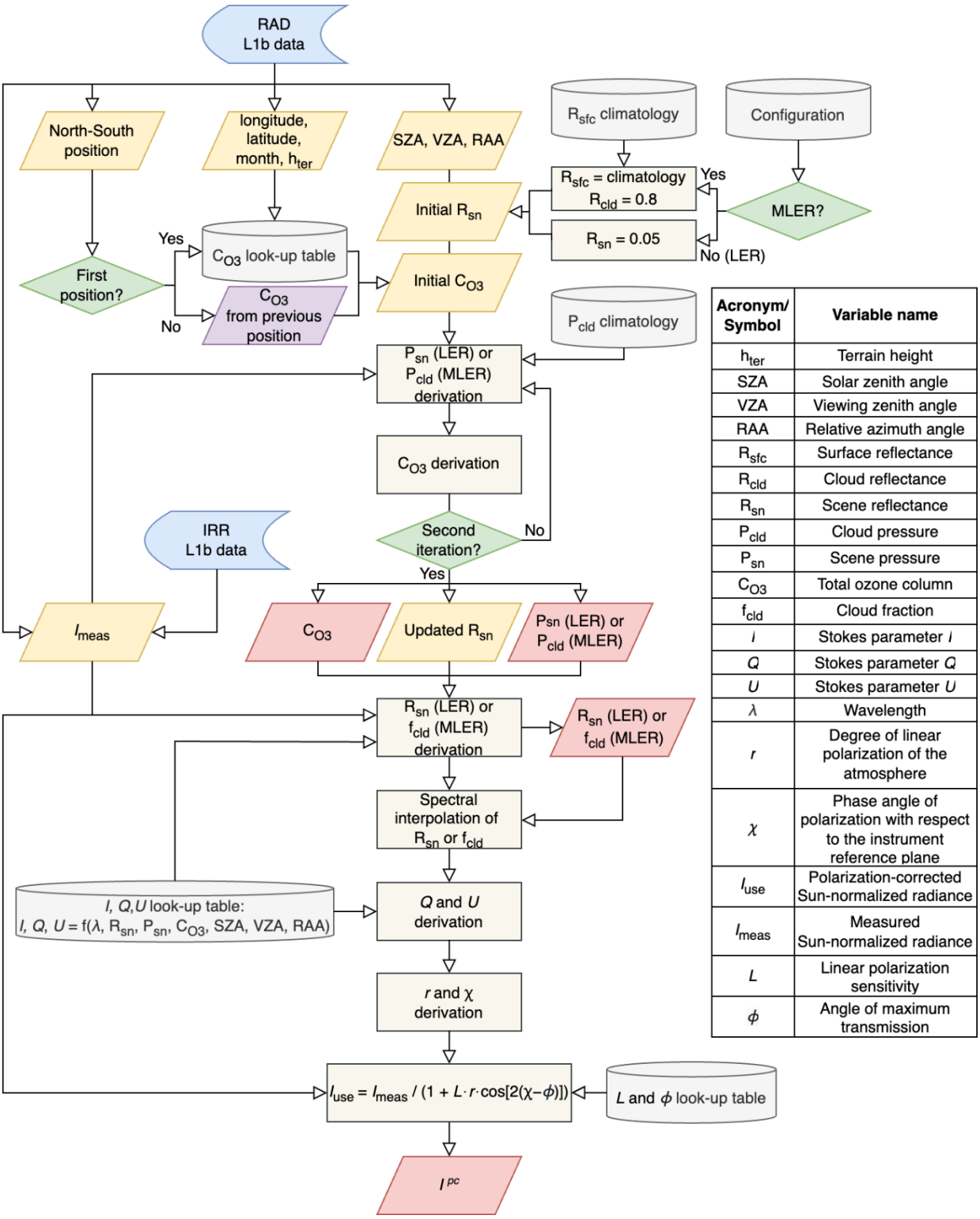

Acronym/ Symbol	Variable name
h_{ter}	Terrain height
SZA	Solar zenith angle
VZA	Viewing zenith angle
RAA	Relative azimuth angle
R_{sfc}	Surface reflectance
R_{cld}	Cloud reflectance
R_{sn}	Scene reflectance
P_{cld}	Cloud pressure
P_{sn}	Scene pressure
C_{O3}	Total ozone column
f_{cld}	Cloud fraction
I	Stokes parameter *I*
Q	Stokes parameter *Q*
U	Stokes parameter *U*
λ	Wavelength
r	Degree of linear polarization of the atmosphere
χ	Phase angle of polarization with respect to the instrument reference plane
I_{use}	Polarization-corrected Sun-normalized radiance
I_{meas}	Measured Sun-normalized radiance
L	Linear polarization sensitivity
ϕ	Angle of maximum transmission

Figure B2. Flow chart of Earth polarization correction.

Acknowledements

TEMPO is NASA's first Earth Venture Instrument (EVI-1) project, led by Smithsonian Astrophysical Observatory (SAO) with project management at NASA Langley Research Center (LaRC) and instrument development at Ball Aerospace (now BAE systems). This study was supported by NASA's TEMPO Grant (NNL13AA09C) and SNWG TEMPO Near Real Time Grant (80MSFC24CA004). The Atmospheric Science Data Center (ASDC) at NASA LaRC supports the archiving and distribution of TEMPO products.

Open Research

The Version 3 TEMPO Level 1 products are available at the NASA Atmospheric Science Data Center (ASDC) via https://asdc.larc.nasa.gov/project/TEMPO. The NOAA/NESDIS IMS Version 1.3 data used for the snow and ice cover derivation are available at https://doi.org/10.7265/N52R3PMC. The GMTED data used for the terrain height calculation are available at https://www.usgs.gov/coastal-changes-and-impacts/gmted2010. The MODIS MCD12Q1 Version 5 data used for the land cover assignment have now been replaced with Version 6.1 data, which are available at https://lpdaac.usgs.gov/products/mcd12q1v061/.

References

Beirle, S., Lampel, J., Lerot, C., Sihler, H., & Wagner, T. (2017). Parameterizing the instrumental spectral response function and its changes by a super-Gaussian and its derivatives. *Atmospheric Measurement Techniques*, 10(2), 581–598. https://doi.org/10.5194/amt-10-581-2017

Burrows, J. P., Weber, M., Buchwitz, M., Rozanov, V., Ladstätter-Weißenmayer, A., Richter, A., et al. (1999). The Global Ozone Monitoring Experiment (GOME): Mission concept and first scientific results. *Journal of the Atmospheric Sciences*, 56(2), 151–175. https://doi.org/10.1175/1520-0469(1999)056<0151:TGOMEG>2.0.CO;2

Bovensmann, H., Burrows, J. P., Buchwitz, M., Frerick, J., Noël, S., Rozanov, V. V., et al. (1999). SCIAMACHY: Mission objectives and measurement modes. *Journal of the Atmospheric Sciences*, 56(2), 127–150. https://doi.org/10.1175/1520-0469(1999)056<0127:SMOAMM>2.0.CO;2

1237 Carr, J. (2016). Image Navigation and Registration (INR) transfer from exquisite systems to
1238 hosted space payloads. US 9,383,210 B2, filed January 30, 2015, published July 5, 2016.
1239 Carr J., Liu, X., Baker, B., & Chance, K. (2017). Observing nightlights from space with TEMPO.
1240 *International Journal of Sustainable Lighting*, 19, 26 – 35.
1241 https://doi.org/10.26607/ijsl.v19i1.64
1242 Carr, J. L., Chong, H., Liu, X., Houck, J. C., Kalb, V., Madani, H., et al. (2025). TEMPO at night.
1243 *Earth and Space Science*, in review.
1244 Chance, K. (1998). Analysis of BrO measurements from the Global Ozone Monitoring
1245 Experiment. *Geophysical Research Letters*, 25(17), 3335–3338.
1246 https://doi.org/10.1029/98GL52359
1247 Chance, K. (2006). Spectroscopic measurements of tropospheric composition from satellite
1248 measurements in the ultraviolet and visible: steps toward continuous pollution monitoring
1249 from space. *NATO Security through Science Series*, 1–25. https://doi.org/10.1007/978-1-
1250 4020-5090-9_1
1251 Choi, H., Liu, X., González Abad, G., Seo, J., Lee, K.-M., & Kim, J. (2021). A fast retrieval of
1252 cloud parameters using a triplet of wavelengths of oxygen dimer band around 477 nm,
1253 *Remote Sensing*, 13(1), 152. https://doi.org/10.3390/rs13010152
1254 Choi, H., Liu, X., Jeong, U., Chong, H., Kim, J., Ahn, M.-H., et al. (2024). Geostationary
1255 Environment Monitoring Spectrometer (GEMS) polarization characteristics and
1256 correction algorithm. *Atmospheric Measurement Techniques*, 17, 145–164.
1257 https://doi.org/10.5194/amt-17-145-2024
1258 Coddington, O. M., Richard, E. C., Harber, D., Pilewskie, P., Woods, T. N., Chance, K., et al.
1259 (2021). The TSIS-1 hybrid solar reference spectrum. *Geophysical Research Letters*, 48,
1260 e2020GL091709. https://doi.org/10.1029/2020GL091709
1261 Coddington, O. M., Richard, E. C., Harber, D., Pilewskie, P., Woods, T. N., Snow, M., et al.
1262 (2023). Version 2 of the TSIS-1 hybrid solar reference spectrum and extension to the full
1263 spectrum. *Earth and Space Science*, 10, e2022EA002637.
1264 https://doi.org/10.1029/2022EA002637
1265 Danielson, J. J. & Gesch, D. B. (2011). Global multi-resolution terrain elevation data 2010
1266 (GMTED2010) [Dataset]. Earth Resources Observation and Science (EROS) Center,
1267 https://doi.org/10.3133/ofr20111073

Friedl, M. A., Sulla-Menashe, D., Tan, B., Schneider, A., Ramankutty, N., Sibley, A., et al. (2010). MODIS Collection 5 global land cover: Algorithm refinements and characterization of new datasets. *Remote Sensing of Environment*, 114(1), 168–182. https://doi.org/10.1016/j.rse.2009.08.016

González Abad, G., Souri, A. H., Bak, J., Chance, K., Flynn, L. E., Krotkov, N. A., et al. (2019). Five decades observing Earth's atmospheric trace gases using ultraviolet and visible backscatter solar radiation from space. *Journal of Quantitative Spectroscopy & Radiative Transfer*, 238, 106478. https://doi.org/10.1016/j.jqsrt.2019.04.030

González Abad, G., Nowlan, C. R., Liu, X., Wang, H., & Chance, K. (2025). TEMPO formaldehyde retrieval algorithm theoretical basis document. https://doi.org/10.5067/D0GI6E8K0NO8

Hou, W., Liu, X., Houck, J., Chong, H., Chan Miller, C., Flittner, D. E., et al. (2025). Spectral calibration for TEMPO (Tropospheric Emissions: Monitoring of Pollution): Algorithm and early results. In preparation.

Kalluri, S., Alcala, C., Carr, J., Griffith, P., Lebair, W., Lindsey, D., et al. (2018). From photons to pixels: Processing data from the advanced baseline imager. *Remote Sensing*, 10(2), 177. https://doi.org/10.3390/rs10020177

Kim, J., Jeong, U., Ahn, M.-H., Kim, J. H., Park, R. J., Lee, H., et al. (2020). New era of air quality monitoring from space: Geostationary Environment Monitoring Spectrometer (GEMS). *Bulletin of the American Meteorological Society*, 101, E1–E11. https://doi.org/10.1175/BAMS-D-18-0013.1

Leitch, J. W., Delker, T., Good, W., Ruppert, L., Murcray, F., Chance, K., et al. (2014). The GeoTASO airborne spectrometer project. *Proc. SPIE 9218, Earth Observing Systems XIX*, 9218. https://doi.org/10.1117/12.2063763

Levelt, P. F., van den Oord, G. H. J., Dobber, M. R., Mälkki, A., Visser, H., de Vries, J., et al. (2006). The Ozone Monitoring Instrument. *IEEE Transactions on Geoscience and Remote Sensing*, 44(5), 1093–1101. https://doi.org/10.1109/TGRS.2006.872333

Munro, R., Lang, R., Klaes, D., Poli, G., Retscher, C., Lindstrot, R., et al. (2016). The GOME-2 instrument on the Metop series of satellites: instrument design, calibration, and level 1 data processing – an overview. *Atmospheric Measurement Techniques*, 9, 1279–1301. https://doi.org/10.5194/amt-9-1279-2016

1299 Nowlan, C. R., González Abad, G., Liu, X., Wang, H., & Chance, K. (2025). TEMPO nitrogen
1300 dioxide retrieval algorithm theoretical basis document.
1301 https://doi.org/10.5067/WX026254FI2U
1302 Park, J., Liu, X., Houck, J., Haffner, D., & Chance, K. (2025). Algorithm description for the
1303 TEMPO total ozone retrieval algorithm.
1304 https://asdc.larc.nasa.gov/documents/tempo/TEMPO_O3TOT_Algorithm_description_V
1305 1.1.pdf
1306 Seftor, C. J., Jaross, G., Kowitt, M., Haken, M., Li, J., & Flynn, L. E. (2014). Postlaunch
1307 performance of the Suomi National Polar-orbiting Partnership Ozone Mapping and
1308 Profiler Suite (OMPS) nadir sensors. *Journal of Geophysical Research: Atmospheres*,
1309 119.(7), 4431–4428. https://doi.org/10.1002/2013JD020467
1310 Sun, J.-Q. & Xiong, X. (2007). MODIS polarization-sensitivity analysis, *IEEE Transactions on*
1311 *Geoscience and Remote Sensing*, 45, 2875–2885.
1312 https://doi.org/10.1109/TGRS.2007.900672
1313 Tan, B., Dellomo, J., Wolfe, R., & Reth, A. (2018). GOES-16 ABI navigation assessment. *Proc.*
1314 *SPIE 10764, Earth Observing Systems XXIII*, 10764, 131–142.
1315 https://doi.org/10.1117/12.2321170
1316 Tilstra, L. G., Tuinder, O. N. E., Wang, P., & Stammes, P. (2017). Surface reflectivity
1317 climatologies from UV to NIR determined from Earth observations by GOME-2 and
1318 SCIAMACHY. *Journal of Geophysical Research: Atmospheres*, 122(7), 4084–4111.
1319 https://doi.org/10.1002/2016JD025940
1320 U.S. National Ice Center (2008). IMS Daily Northern Hemisphere Snow and Ice Analysis at 1
1321 km, 4 km, and 24 km Resolutions, Version 1 [Dataset]. Boulder, CO, USA, National
1322 Snow and Ice Data Center (NSIDC), https://doi.org/10.7265/N52R3PMC
1323 Veefkind, J. P., Aben, I., McMullan, K., Förster, H., de Vries, J., Otter, G., et al. (2012).
1324 TROPOMI on the ESA Sentinel-5 Precursor: A GMES mission for global observations of
1325 the atmospheric composition for climate, air quality and ozone layer applications. *Remote*
1326 *Sensing of Environment*, 120, 70–83. https://doi.org/10.1016/j.rse.2011.09.027
1327 Wang, H., Nowlan, C. R., González Abad, G., Chong, H., Hou, W., Houck, J. C., et al. (2025).
1328 Algorithm theoretical basis for Version 3 TEMPO O_2-O_2 cloud product. *Earth and Space*
1329 *Science*, 12, e2024EA004165. https://doi.org/10.1029/2024EA004165

1330 Zong, Y., Brown, S. W., Meister, G., Barnes, R. A., & Lykke, K. R. (2007). Characterization and
1331 correction of stray light in optical instruments. *Proc. of SPIE*, 6744,
1332 https://doi.org/10.1117/12.737315
1333 Zoogman, P., Liu, X., Suleiman, R. M., Pennington, W. F., Flittner, D. E., Al-Saadi, J. A., et al.
1334 (2017). Tropospheric Emissions: Monitoring of Pollution (TEMPO). *Journal of*
1335 *Quantitative Spectroscopy and Radiative Transfer*, 186, 17–39.
1336 https://doi.org/10.1016/j.jqsrt.2016.05.008